Institute of Atmospheric Physics

Deutsches Zentrum
für Luft- und Raumfahrt
German Aerospace Center

DLR e. V. Institute of Atmospheric Physics
Oberpfaffenhofen, Postfach 11 16, 82230 Wessling, Germany

Atmospheric Chemistry and Physics
Board of Editors

Your reference
Your letter
Our reference

Your correspondent Romy Heller

Telephone +49 8153 28- 2563
Telefax +49 8153 28- 1841
E-mail romy.heller@dlr.de

6 October 2017

Publication of the manuscript "Mountain waves modulate the water vapor distribution in the UTLS"

Dear Jörg Gumbel,

In our manuscript "Mountain waves modulate the water vapor distribution in the UTLS", we present a new approach to quantify location, direction and irreversibility of the water vapor transport during a strong mountain wave event observed during the field campaign DEEPWAVE in 2014. This is a revision of the manuscript published in ACPD including changes suggested by the reviewers of the first version.

We include a discussion of the Scorer parameter profile determined from dropsondes to give an additional explanation of the observed horizontal wavelengths that are responsible for a vertical water vapor flux. Though, we defined water vapor as passive tracer in our case study, we now give a more detailed discussion on observed lee waves at a low altitude and their possible influence on the vertical water vapor flux calculation. Due to the non-existence of a realistic vertical water vapor profile in the mountain wave region, we decided to leave out a comment on the mixing effectiveness in the manuscript. In the part regarding the atmospheric radiation budget we moderate our statement and discuss uncertainties resulting from our estimation of the local radiative forcing based on a study of zonally and annually averaged water vapor distributions by Riese et al. (2012).

We have added Andreas Giez and Christian Mallaun from DLR Flight Experiments to the author's list. They were responsible for the measurement and data evaluation of the meteorological parameters on board the DLR Falcon aircraft during the DEEPWAVE campaign. Especially, the vertical wind measurements were used for the calculations of the vertical water vapor flux in the manuscript.

We believe that the new version of the manuscript suits the journal's criteria of high-impact, innovative and timely research with immediate implications on the work of others. Our study can be used for data analysis of field campaigns with similar research topics and the described methods are suitable for other trace species with a strong gradient in the UTLS as well.

All authors have approved to the submission of the manuscript and its contents have not been submitted or published elsewhere.

We hope you find the new version of the manuscript interesting and adequate for publication in your journal.

Sincerely,

Romy Heller

Oberpfaffenhofen
Muenchener Str. 20
82234 Wessling, Germany
Telephone +49 8153 28-0
Internet DLR.de

Response to Anonymous Referee #1 (acp-2017-334-RC1)

Our responses are written in italic.

The changes in the manuscript are transferred and marked as quotations.

We thank the reviewer for his/her positive assessment of the manuscript and the helpful comments.

The authors present an interesting case study addressing vertical transport and irreversible mixing of water vapor in the UTLS associated with a mountain wave event …

The paper is clearly of interest, as trace gas and particularly water vapor transport by mountain waves followed by irreversible mixing is little understood and represents a source of uncertainty in simulations. The presented set of observations supports a consistent picture of local upward transport by mountain waves and partial mixing, resulting in a net enhancement of water vapor in the tropopause region. The estimated radiative forcing should be taken with care, since local observations at a certain time of the year are combined with zonally and temporally averaged data. As indicated by the authors, this aspect clearly requires further studies. The paper is clear-written and well structured. The study should be published in ACP after clarification of some minor points:

P 5 line 16 and elsewhere: cloud-free conditions, water as conservative tracer: As potential condensation may influence the analysis, the absence of (thin) clouds should be assured using airborne data (e.g. particle observations or temperature). Later it is said that ice particles were detected at the leewave side. What is the detection limit for condensed water? Could significant amounts of condensed water be missed, or can this be ruled out?

We detected cirrus clouds during the campaign by measuring total water with a tunable diode laser hygrometer with a forward-facing inlet. We calculated the ice water content by subtracting the saturation mixing ratio from the total water signal and correction for particle enhancement. The resulting detection limit for the ice water content is 0.2 ppmv. The clouds in the lee of the New Zealand Alps that are mentioned in the manuscript had an ice water content of 10 to 200 ppmv and were observed on the lowest flight leg (7.7 km) of the first Falcon flight. This is in agreement with satellite measurements. No clouds were observed at higher flight altitudes of this flight and during the second Falcon flight. The possible influence of these clouds is discussed in the manuscript.

"For the flux calculations we used water vapor as conservative tracer due to the absence of supersaturation at the analysed flight altitudes. However, at the first flight leg of FF04 at 7.7 km we measured ice particles with the in-situ instrumentation with a detection limit for the ice water content of 0.2 ppmv. The cloud was detected between +150 km and +200 km distance and indicates the existence of a lee wave cirrus. This gravity wave induced cloud was also visible in the infra-red images of the MTSAT-2 satellite at 03 UTC and dissipated until 06 UTC (Bramberger et al., 2017). No further clouds were measured on the other flight legs and in particular not during those legs for which the flux calculations were performed. However, the presence of an ice cloud on a lower layer may affect the water vapor distribution at a higher flight level (8.9 km) by lowering the amplitude of the fluctuation. In Figure 3 we observe a strong negative peak in the vertical wind at +170 km distance to the summit in contrast to a small water vapor fluctuation which may be influenced by the drying of the level below. The calculated flux in this region is then also reduced. This effect does not influence the general transport direction at this flight altitude and is not relevant for the higher flight altitudes or the second Falcon flight since these lee wave clouds were not observed above 7.7 km and dissipated during the first flight."

P 5 line 28: To me it was sometimes difficult to connect the flight legs and locations/ directions with the map in Fig. 1. As Mt. Aspiring serves as reference point, coordinates should be provided in the text and it would be helpful to mark this point in the maps.

In the revised manuscript we have marked Mt. Aspiring in Fig. 1 and have provided the coordinates.

P8 sect. 4.1 and Figure 1: As the vertical domain is in the focus of this study and locations are relevant, it may be helpful to add a vertical cross section of vertical wind from the model along the cross-mountain flight path and indicate the flight legs.

We now have added a vertical cross section of the vertical wind in Fig. 1 and have marked the flight leg for which model calculations were carried out for better clarity.

P12 line 4, Figure 6: While the data suggest upward transport through the thermal tropopause, it would be interesting to include comment on the dynamical tropopause. Are thermal and dynamical tropopause approximately coincident here? Furthermore, how is the approximate thermal tropopause location determined in Figure 6 (dropsondes/model)? Could the location be biased by temperature signatures of the strong waves?

The height of the thermal tropopause on 4 July 2014 was determined by output of numerical weather prediction models (ECMWF and WRF). These findings were confirmed by analyzing the dropsonde temperature profiles. The dynamical tropopause was derived as the 2-PVU level in the WRF model data. It is approximately coincident with the thermal tropopause, i.e., it is just located a few hundred meters below. In the region of the observed mountain waves the tropopause (thermal as well as dynamical) is more structured and potentially biased by wave signatures than up- or downstream the mountains. Therefore, the given heights of the tropopause are averages over the whole flight leg distance.

P12 line 6, Figure 6b: exact localization of maxima : : : not possible: It is clear that it is difficult to have observations at many different levels in a short time window and here the best possible is done. However, could the pattern in Figure 6b change significantly if more/other levels would be available?

We added a short note on this discussion topic. The first Falcon flight shows the same pattern of vertical divergence for the lower altitudes. A significant change should not appear by using other levels, but maxima could possibly shift in altitude. In another field campaign conducted two years after DEEPWAVE, a lidar for water vapor measurements pointed upward and made it possible to derive a profile of the vertical water vapor flux. However, the operating lidar instruments on board the Falcon and the GV were not measuring water vapor during DEEPWAVE.

"For the first Falcon flight we find a similar pattern and values for the flux divergence between 7.7 and 10.8 km (Table 3). The use of other levels could change the pattern slightly but the general trend appears to be robust. Vertically resolved data (e.g. by lidar measurements) would be required to derive the vertical curtain of the flux divergence but were not performed during this campaign."

P13 line 25: Turbulence is identified in the dropsonde data between 329 and 334 K and suggests mixing. Figure 7b shows that the situation is changing within hours. Is it robust to apply this potential temperature range from a single dropsonde profile to the H2O-O3 correlation from a full flight covering several hours?

We clarify this remark. The potential temperature range of 329 to 334 K for turbulence is derived from a total of 9 dropsonde launches during the GV flight. These dropsondes were launched over 5 hours so we assume a similar range for the first Falcon flight. The altitude range of the turbulence occurence changed due to a change in the tropopause height.

"The layers of suggested turbulence, found in all nine dropsondes launched above the middle and eastern part of the mountains, generally have a thickness of approximately 200 m and are correlated with a potential temperature range of 329 to 334 K."

"The dropsondes, covering a time range of 5 hours before, during and after the second Falcon flight FF05, always show turbulence in the same potential temperature range with slight changes in the altitude due to the descent of the thermal tropopause. Thus, we also assume the presence of turbulence layers for similar potential temperatures during the first Falcon flight FF04."

P13 line 21: A local _ 1 W/m2 radiative forcing is estimated locally above New Zealand in July. However, Figure 6 in Riese et al. (2012) refers to annually and zonally averaged values. How could this affect this estimate?

We have tried to moderate our statement by emphasizing the difference between our own study and the study of Riese et al. (2012). We attempted to relate the results of Riese et al. (2012) to our measurement region and then derived a lower limit for the radiative effect. Since we compare our case for mixing by mountain waves with annually and zonally averaged values a large uncertainty exist. Water vapor shows a seasonality in the mid latitude region of the Southern Hemisphere (e.g. Hegglin et al., 2013[1]) with lower mixing ratios in July than in January. The use of absolute values for the difference in the water vapor mixing ratio induced by mixing would lead to a biased estimation of the radiative forcing. However, we based our estimation on the percentage difference which slightly reduces the uncertainty for a comparison of annually averaged mixing ratios with a case on a specific day.

"Under the assumption that the simulated difference in the distribution of water vapor as a result of enhanced mixing may also be representative for our case of mixing induced by mountain waves, we estimate a radiative forcing larger than 1 W m^{-2} locally above New Zealand during and after the mountain wave event. Riese et al. (2012) do not give a physical reason for the changes in the mixing strength, so our case may present a physical process (among other processes) contributing to the change in the water vapor distribution in the UTLS. While we used the calculations by Riese et al. (2012) at the measurement location, their study has a coarser vertical and horizontal resolution and is averaged over one year. We here neglect the seasonality in the water vapor mixing ratio that is present in the southern hemisphere at this latitude range. Thus, our estimate has a large uncertainty. Nevertheless, it emphasizes the relevance of mountain waves on the water vapor distribution and the radiation budget of the UTLS."

[1] Hegglin, M. I., Tegtmeier, S., Anderson, J., Froidevaux, L., Fuller, R., Funke, B., Jones, A., Lingenfelser, G., Lumpe, J., Pendlebury, D., Remsberg, E., Rozanov, A., Toohey, M., Urban, J., von Clarmann, T., Walker, K. A., Wang, R., and Weigel, K.: SPARC Data Initiative: Comparison of water vapor climatologies from international satellite limb sounders, J. Geophys. Res. Atmos., 118(20), 11,824-811,846, doi:10.1002/jgrd.50752, 2013.

Technical:

Thank you for the following remarks; they are now corrected in the manuscript.

P3 line 3: correlations

P6 Eqns 1 and 2: define x and t

P9 line 18: check number/unit: -176 m ppmv

P9 line 28: strong negative peak

Figure 5: numbers at right y-axes of panels on the right side would be helpful

Response to Anonymous Referee #2 (acp-2017-334-RC2)

Our responses are written in italic.

The changes in the manuscript are transferred and marked as quotations.

We thank the reviewer for his/her helpful comments and suggestions to improve the manuscript.

This study addresses the modulation of water vapour in the upper troposphere/lower stratosphere by mountain waves. It draws on a wealth of aircraft measurements made over New Zealand in the context of the DEEPWAVE campaign, and puts them to good use, combined with numerical simulations and soundings. The paper contains a rather thorough processing of these data (for example, using wavelet analysis), with the aim of understanding how mountain waves influence the behaviour of atmospheric water vapour near the tropopause. The work is highly relevant scientifically, namely because it reports on novel data, and may have climate implications, and is suitable for the scope of ACP. Both previous work on the topic and the scientific approach and methods are adequate and discussed in appropriate detail. The number of figures, tables and references included also seems appropriate. The conclusions presented are interesting, relevant and supported by the results. The manuscript is well organized and written in good-quality, clear English.

General comments

Since, as pointed out by the authors, the fluctuations of water vapour in an atmosphere with strong gradients of this substance can be explained using a mixing-length argument, it would be nice to see how well the mixing length obtained from this kind of argument (i.e. defined as the magnitude of the water vapour fluctuations divided by the water vapour gradient) compares with the wave amplitude obtained directly from integrating the vertical velocity. This would, presumably, give indications about the mixing effectiveness, as a mixing length substantially smaller than the diagnosed wave amplitude would suggest considerable fluid parcel dilution.

We fully agree with the reviewer that a calculation of the mixing length and comparison to the wave amplitude would be useful to evaluate the mixing effectiveness. However, the calculation of a mixing length is not possible since we do not have a realistic water vapor profile over the mountains. During the analysis of this case study we thought about calculating the

vertical exchange coefficient K_q ($K_q = -\frac{\overline{w'q'}}{\frac{d\bar{q}}{dz}}$) that is similar to the mixing length argument you mentioned ($\frac{\overline{q'}}{\frac{d\bar{q}}{dz}}$) but for both methods a vertical gradient of H_2O is necessary. From our in-situ measurements of water vapor on the Falcon and on the GV we derived an approximate profile from ascent and descent and from changes between the flight levels upstream or downstream the mountains. In the region of the observed mountain waves no vertical water vapor profile exists. Also, we cannot use the water vapor profile from the dropsondes since they were launched at 12.2 km altitude and the humidity sensor does not work properly 2 to 3 km below the launch altitude (very low humidity in tropopause region). A vertical profile of water vapor from model simulations (ECMWF, WRF) is also not applicable because the humidity of the models and the in-situ measurement in the tropopause region shows discrepancies in absolute values and in the amplitude of the fluctuations. A detailed comparison would be necessary. Additionally, we tested a method to determine the vertical gradient of water vapor from a correlation between the vertical displacement and the water vapor fluctuations on each flight leg. The method was adapted from Smith et al. (2008)[2] displayed in their Fig. 9 and eq. 3. The vertical gradient of water vapor can be estimated from the slope of the linear relation between vertical displacement and water vapor fluctuations. However, the correlation scattered too much to derive a linear relationship between the two parameters. Thus, a vertical gradient of water vapor in the sensitive tropopause region has a large uncertainty. Due to this fact, we decided to leave out the discussion on the mixing effectiveness from the manuscript.

In Section 5 and Figure 7, some attention is devoted to the vertical profiles of the potential temperature theta and the wind velocity (U, V), for the purpose of calculating the Richardson number Ri. Although this is obviously highly relevant from the standpoint of turbulence generation, it would also be interesting to add panels to Figure 7 containing Scorer parameter profiles, computed from the same quantities, and discuss the implications of the vertical structure of these profiles in terms of vertical propagation (or trapping) and amplification (or decay) of the mountain waves.

We are grateful for this comment that gives an additional and interesting statement to our manuscript by explaining the observed wavelengths that are responsible for a vertical water vapor flux. The profile of the Scorer parameter is similar for all dropsondes launched during the flight RF16. It shows that linear gravity waves with horizontal wavelengths larger than 10 to 20 km can vertically propagate in the troposphere if they are excited by the flow over the mountain. In the middle and upper troposphere, the critical wavelength increases slightly resulting in an evanescent behavior for horizontal wavelengths smaller than about 22 km. These results of the vertical dependence of the Scorer parameter confirm our observations of horizontal wavelengths larger than 20 km that transport water vapor upward or downward.

[2] Smith, R. B., Woods, B. K., Jensen, J., Cooper, W. A., Doyle, J. D., Jiang, Q. F., and Grubisic, V.: Mountain waves entering the stratosphere, J. Atmos. Sci., 65(8), 2543-2562, doi:10.1175/2007jas2598.1, 2008.

“Another characteristic factor is the Scorer parameter ℓ that is shown in Figure 7c for the dropsonde launched at 07:55 UTC (44.39°S, 169.60°E) The Scorer parameter is used to estimate the critical horizontal wavelengths allowing vertical propagation of linear gravity waves under the given atmospheric conditions. The vertical profile of ℓ shows that gravity waves with horizontal wavelengths between 10 and 20 km are able to propagate vertically if they are excited in the lower troposphere. Between 4 and 9 km altitude, wave modes with horizontal wavelengths smaller than the critical wavelength of about 22 km become evanescent and may be attenuated. The magnitude of the estimated critical wavelength based on the Scorer parameter confirms our observations in the power spectra and wavelet cospectrum (Figure 5): the upward transport of water vapor is dominated by horizontal wavelengths larger than 22 km. A downward transport is possible by wavelengths smaller than 22 km due to a wave attenuation in the upper troposphere that is responsible for damping and partial reflecting of gravity waves. The vertical profile of ℓ is similar for all dropsonde launches (upstream and over the mountains) and is also comparable to an upstream ℓ-profile from the IFS forecast shown in Figure 3b in Bramberger et al. (2017).“

Specific comments

Page 2, Lines 23-24: "The transport of trace gas species may be reversible or irreversible, depending on mixing processes on different scales.". This sentence as it stands could be misleading. Any mixing will cause irreversibility, yet the reader gets the impression that reversibility depends on the scale at which mixing occurs. Consider rephrasing to clarify.

We agree and have rephrased the sentence to clarify the issue of (ir)reversibility of transport processes.

Page 3, lines 3-4: "The tracer-tracer correlation are based on a dynamic approach". Please replace "correlation" with "correlations". What is meant by "dynamic approach here? Is the purpose simply making a contrast with "microphysics" mentioned later in the sentence? If yes, this should be better explained.

We refer to dynamic transport processes as the main reason for the behavior of the tracer-tracer correlations and make clear that water vapor is special due to additional microphysical processes (cloud formation and freezing out of water vapor).

“In addition to transport and mixing processes, in cloudy situations, the tracer-tracer correlations for water vapor may additionally be affected by microphysical processes and cloud formation. Then, effects of clouds on the correlations have to be discussed in such situations.”

Page 7, line 20: "with a lag of one and a lag of 10". It is not obvious to the reader why these values are used. Perhaps the authors should cite here (again) the reference where these assumptions are motivated.

The used autocorrelation factor in eq. 9 is determined by the method of Portele et al. (2017) in the way that large and small wavelengths are weighted similarly to be significant.

"The original time series is correlated with a delayed copy of itself (time lag) to obtain the significant parts of the cospectrum. The chosen combination includes signals of larger wavelengths (significant for high time lags) and smaller wavelengths (significant for lower lags) without stressing any of them (Portele et al., 2017)."

Page 11, lines 6-9: "In their study flux-carrying waves are larger than 20km horizontal wavelength. Small scale waves with wavelengths around 20km and less are mainly dominating in the vertical wind motion and do not carry any energy or momentum flux upward". It should be noted that, in the case of momentum or energy, the reason for this behaviour is dynamical, since only large-scale waves that propagate vertically (i.e. are not evanescent) transport momentum and energy vertically. For water vapour, this scale filtering cannot occur for the same reasons, since water vapour may be viewed as an essentially passive tracer.

We thank for this remark and agree that there are dynamical reasons for the behavior of the energy and momentum flux. Nevertheless, for this wavelength scale range (20 – 80 km) water vapor is a passive tracer for this wave dynamics. Since we use similar equation for the flux calculations the scale separation for momentum and energy transport is comparable to that for the trace gas transport. For larger scales (>100 km) other processes would be dominant but this is not in the scope of this analysis.

"In the statistical analysis of all GV flight level data during DEEPWAVE, Smith et al. (2016) also observed small and longer scale waves with different characteristics. In their study flux-carrying waves are larger than 20 km horizontal wavelength. Small scale waves with wavelengths around 20 km and less are mainly dominating in the vertical wind motion and do not carry any energy or momentum flux upward (Smith & Kruse, 2017). This is explained by dynamic reasons since only the longer-scale waves that propagate vertically and are not evanescent transport energy and momentum vertically. For water vapor as passive tracer the reasons for the chosen scale separation are the same in this wavelength range. Transport processes by large-scale waves with horizontal wavelengths larger than 100 km would be presumably different for energy or momentum and water vapor."

Page 14, lines 19-22: "Under the assumption that the change in the climatological distribution of water vapour may also be representative for our case of mixing induced by mountain waves, we estimate a radiative forcing > 1 W m^-2 locally above

New Zealand during and after the mountain wave event.". It would be good to discuss the validity of this assumption a bit further. Under what circumstances is it expected to fail?

We discuss our assumption in more detail and emphasize the difference between our case and the study of Riese et al. (2012). For our estimation we use the same latitude range and altitude. Nevertheless, a large uncertainty exists since Riese et al. (2012) has a coarser resolution in vertical and horizontal dimension and is based on zonally and annually averaged values. Additionally, our assumption is expected to fail in the absence of permanent mixing.

"Under the assumption that the simulated difference in the distribution of water vapor as a result of enhanced mixing may also be representative for our case of mixing induced by mountain waves, we estimate a radiative forcing larger than 1 W m^{-2} locally above New Zealand during and after the mountain wave event. Riese et al. (2012) do not give a physical reason for the changes in the mixing strength, so our case may present a physical process (among other processes) contributing to the change in the water vapor distribution in the UTLS. While we used the calculations by Riese et al. (2012) at the measurement location, their study has a coarser vertical and horizontal resolution and is averaged over one year. We here neglect the seasonality in the water vapor mixing ratio that is present in the southern hemisphere at this latitude range. Thus, our estimate has a large uncertainty. Nevertheless, it emphasizes the relevance of mountain waves on the water vapor distribution and the radiation budget of the UTLS."

Page 14, lines 27-28: "Further studies are required to evaluate the radiative forcing caused by changes in the water vapor mixing ratios due to gravity waves in more detail and/or on larger scales.". Why specifically on larger scales? What scales in particular?

We have removed the remark on larger scales (horizontal wavelengths larger than 100 km). The flux calculations refer to horizontal wavelengths smaller than 80 km but in the H_2O-O_3 correlation all wavelength scales are included. Therefore, our estimation on the radiative forcing covers all wavelength scales. A separation of the impact of different wavelength scales on the radiative forcing would be difficult and is beyond the scope of this study.

Page 16, lines 4-6: "The locally and temporally limited radiative forcing over the Southern Alps exceeded 1 W mˆ-2 and suggests that mountain waves may have a large effect on climate.". I suspect this may be an overstatement. To ascertain whether this claim is reasonable, the prevalence of mountain waves similar to those addressed in the present study would have to be taken into account. The tone of this remark could be moderated.

We have moderated the tone in this statement according to the reviewer's suggestion. To our knowledge, this is the first study that estimates a radiative forcing in the context of a local mountain wave event. Since we have several mountain wave hot

spots all over the world a study of the influence of mixing caused by these mountain waves on the radiation budget in the UTLS would be interesting.

"The enhanced water vapor mixing ratios in the tropopause region strongly influences the radiative transfer in the UTLS. The estimated radiative forcing for our case, locally and temporally limited over the Southern Alps of New Zealand, exceeded 1 W m^{-2} and suggests that mountain waves occurring in many locations all over the world may have a non-negligible effect on climate."

Page 28, Figure 4: I do not think the large negative flux of water vapour that can be seen in the bottom graph between x=-50 km and x=+50 km is discussed in sufficient detail in the text. This is an intriguing feature, which may seem puzzling to the reader. I advise the authors to include an interpretation of it, even if speculative, justifying its intensity, location and extent.

We now have addressed this issue with an explanation regarding the tropospheric jet stream influence in this region. In Fig. 3 a decrease in the water vapor mixing ratio together with an increase in the potential temperature und changes in the horizontal wind components indicate an impact of the tropospheric jet stream between -50 and + 50 km distance that is also visible in the synoptic plots of Fig. 1. The vertical wind component is not influenced by the jet stream. Since the decrease in water vapor cannot fully be eliminated by the used filter to obtain the water vapor perturbation we see this issue in the water vapor flux.

"At the western edge of the mountains (between -50 and +30 km) we also observe a negative flux. This region is located in the vicinity of the tropospheric jet stream which influences the distribution of the water vapor mixing ratio by horizontal transport processes (Figure 3: decrease of H_2O from west to east between -80 km and 0 km distance). This behavior cannot fully be eliminated by the used filter and is thus present in the water vapor perturbations by a few fluctuations with a negative weighting."

Page 30, Figure 6: In panel(a), the caption does not explain what the red dashed lines represent. Please add that information. In panel (b), the dotted line corresponding to the water vapour flux filtered for waves with wavelengths between 20 km and 80 km does not include a point at z=7.7 km, but the solid line does. Why is that? This choice should be justified convincingly in the text.

We have added the definition for the red dashed lines. In panel (b) we now mark the two lines by different line character and different symbol to clarify that we show both wavelengths at each altitude point. At 7.7 km the values for both wavelengths are very similar which was not obvious in the first version of the plot.

Technical corrections

Page 1, Line 13 in Abstract: "GV research aircraft". Does "GV" stand for anything, or is it just the name of the aircraft? In the first possibility, please expand and explain the acronym.

The acronym is now explained in the text.

Page 7, line 9: "q=H_2 O". If the two notations are equivalent, why use "H_2 O" instead of the shorter and more convenient notation "q", as is done throughout the manuscript? Is there any particular reason for this?

We now use "q" in the whole method description section.

Page 11, lines 29-30: "By the absence of vertical or horizontal transport and the existence of a well-mixed atmosphere, we are expecting no flux divergence.". This sentence does not sound very well. Consider rephrasing.

We have rephrased the sentence.

Page 25, Figure 1(b): Is this simply a magnification of Figure 1(a)? If yes, this should be mentioned in the caption.

Fig. 1(b) is a magnification of Fig. 1(a) which is now mentioned in the caption.

Page 26, caption of Figure 2: "... and topography are shown". It would be good to indicate what denotes the topography, i.e. the grey area at the bottom (as done in e.g. Figure 5).

We have added this remark.

Page 27, caption of Figure 3: "the diagonal blue dashed lines in the bottom panel display the phase shift between the vertical wind motion and perturbations in water vapor and theta". It is not totally clear what this means. Does the phase shift correspond to the horizontal distance between the bottom and top of these lines? Please clarify.

We have rephrased the sentence to clarify the meaning of the phase shift.

Mountain waves modulate the water vapor distribution in the UTLS

Romy Heller[1], Christiane Voigt[1,2], Stuart Beaton[3], Andreas Dörnbrack[1], Andreas Giez[4], Stefan Kaufmann[1], Christian Mallaun[4], Hans Schlager[1], Johannes Wagner[1], Kate Young[3], Markus Rapp[1,5]

[1]Deutsches Zentrum für Luft- und Raumfahrt, Institut für Physik der Atmosphäre, Oberpfaffenhofen, Germany
[2]Johannes-Gutenberg-Universität Mainz, Institut für Physik der Atmosphäre, Mainz, Germany
[3]National Center for Atmospheric Research, Boulder, Colorado, USA
[4]Deutsches Zentrum für Luft- und Raumfahrt, Flugexperimente, Oberpfaffenhofen, Germany
[5~~4~~]Ludwig-Maximillians-Universität München, Meteorologisches Institut München, Munich, Germany

Correspondence to: Christiane Voigt (Christiane.Voigt@dlr.de)

Abstract. The water vapor distribution in the upper troposphere/lower stratosphere region (UTLS) has a strong impact on the atmospheric radiation budget. Transport and mixing processes on different scales mainly determine the water vapor concentration in the UTLS. Here, we investigate the effect of mountain waves on the vertical transport and mixing of water vapor. For this purpose we analyse measurements of water vapor and meteorological parameters recorded by the DLR Falcon and NSF/NCAR Gulfstream 5~~GV~~ research aircraft taken during the Deep Propagating Gravity Wave Experiment (DEEPWAVE) in New Zealand. By combining different methods, we develop a new approach to quantify location, direction and irreversibility of the water vapor transport during a strong mountain wave event on 4 July 2014. A large positive vertical water vapor flux is detected above the Southern Alps extending from the troposphere to the stratosphere in the altitude range between 7.7 and 13.0 km. Wavelet analysis for the 8.9 km altitude level shows that the enhanced upward water vapor transport above the mountains is caused by mountain waves with horizontal wavelengths between 22 and 60 km. A downward transport of water vapor with 22 km wavelength is observed in the lee-side of the mountain ridge. While it is a priori not clear whether the observed fluxes are irreversible, low Richardson numbers derived from dropsonde data indicate enhanced turbulence in the tropopause region related to the mountain wave event. Together with the analysis of the water vapor to ozone correlation we find indications for vertical transport followed by irreversible mixing of water vapor.

For our case study, we further estimate greater than 1 W m^{-2} radiative forcing by the increased water vapor concentrations in the UTLS above the Southern Alps of New Zealand resulting from mountain waves relative to unperturbed conditions. Hence, mountain waves have a great potential to affect the water vapor distribution in the UTLS. Our regional study may motivate further investigations of the global effects of mountain waves on the UTLS water vapor distributions and its radiative effects.

1 Introduction

Water vapor is a major greenhouse gas in the UTLS (Sherwood et al., 2010; Solomon et al., 2010). Thus, changes in the water vapor distribution in the UTLS cause a radiative forcing and may affect surface temperatures (Solomon et al., 2010; Riese et al., 2012). Therefore, understanding of sources and sinks as well as transport and mixing of water vapor (Holton et al., 1995; Gettelman et al., 2011) is fundamental to quantify its impact on the atmospheric radiation budget.

There are a few studies that refer to trace gas transport induced by gravity waves (e.g. Danielsen et al., 1991; Langford et al., 1996; Schilling et al., 1999; Moustaoui et al., 2010). Gravity waves are known to play an important role for circulation, structure and variability of the atmosphere (Fritts & Alexander, 2003). They distribute energy and momentum horizontally and vertically in the atmosphere (e.g. Smith et al., 2008; Geller et al., 2013; Wright et al., 2016). The vertical displacement of an air parcel by gravity waves creates fluctuations in trace gas concentrations at constant altitude if the trace gas distribution has a vertical gradient (Smith et al., 2008). For adiabatic processes tracer mixing ratios as well as the potential temperature are thereby conserved. With respect to an analysis of an adiabatic process, water vapor may serve as an excellent tracer for gravity waves in the troposphere to the lower stratosphere region, while for example ozone is a good tracer for the stratosphere. Previous studies investigated the effects of gravity waves on the ozone or carbon monoxide distribution (e.g. Langford et al., 1996; Teitelbaum et al., 1996; Schilling et al., 1999; Moustaoui et al., 2010), while the effects on water vapor are less discussed due to the complex interaction of sources and sinks of water vapor in the UTLS region, for example the possibility of condensation (Moustaoui et al., 1999; Pavelin et al., 2002). Schilling et al. (1999) measured strong fluctuations in CO mixing ratios at a constant flight level (11.9 km) caused by mountain waves and calculated the vertical trace gas flux at this altitude. They derived an upward transport of CO that resulted in enhanced CO mixing ratios at a higher altitude (12.5 km). They speculated that dynamic instabilities were induced by wave breaking and that convective overturning finally led to an irreversible vertical CO transport.

The method to calculate the vertical trace gas flux (Shapiro, 1980; Schilling et al., 1999) is similar to the calculations of energy and momentum fluxes (e.g. by Smith et al., 2008) and indicates the vertical transport direction of the trace gas. If we assume a negative gradient for the trace gas, a positive flux generally will indicate an upward transport of high mixing ratios into a region with low mixing ratios. However, it may also display a downward transport from a region of low mixing ratios to a region with higher mixing ratios (e.g. by existence of an inversion layer). The transport of trace gas species may be reversible or irreversible, depending on ~~mixing~~ processes occurring on different scales. Irreversible mixing is promoted by turbulence induced, for example, by nonlinear wave interaction, wave breaking, or dissipation (Lamarque et al., 1996; Whiteway et al., 2003; Koch et al., 2005; Lane & Sharman, 2006). Danielsen et al. (1991) showed that waves with large horizontal wavelengths (~36 – 270 km) and enhanced vertical amplitudes are significant carriers of energy, momentum and trace species. Small-scale waves (horizontal wavelength smaller than 30 km) may cause mixing and thus enable the irreversibility of the transport induced by large-scale waves. In a later study, Moustaoui et al. (2010) showed that small-scale waves can also be effective in transport based on reversible dynamic processes.

One method to investigate mixing of trace gases in the UTLS region is to consider the correlation between a tropospheric and a stratospheric tracer (e.g Fischer et al., 2000; Hoor et al., 2002; 2004; Pan et al., 2007). In an idealized non-mixed atmosphere, a tropospheric tracer (e.g. H_2O) and a stratospheric tracer (e.g. O_3) are not correlated and show a “L-shape” in a 2D tracer-tracer-plot. Mixing processes across the tropopause (for example by troposphere-stratosphere-transport related to tropopause folds or convection) can lead to linear relations (mixing lines) between the tracers. This feature is observed only for irreversible ~~mixing~~transport. The strength of the mixing and thus the slope of the mixing line is a function of the tracer distributions in the

initial air mass and the elapsed time since the mixing took place (Hoor et al., 2002). ~~The tracer-tracer correlation are based on a dynamic approach but may be affected by microphysics in the case of water vapor.~~In addition to transport and mixing processes, in cloudy situations, the tracer-tracer correlations for water vapor may additionally be affected by microphysical processes and cloud formation. Then, effects of clouds on the correlations have to be discussed in such situations. The consequences of condensation in the tropopause region are not completely displayed in such a correlation plot.

The objective of this paper is to investigate transport of water vapor during a strong mountain wave event using a new combination of different techniques common in gravity wave and atmospheric transport analysis. While previous studies focused on single altitudes, we use measurements in the altitude range between 7.7 km and 13.0 km to cover the upper troposphere and lower stratosphere including the tropopause region. In contrast to previous studies, which mainly applied simulations (Schilling et al., 1999; Moustaoui et al., 2010), here we investigate the irreversibility of the water vapor transport by using in-situ information from tracer-tracer correlations and vertical dropsonde profiles. Furthermore, we are interested in a possible impact of the water vapor distribution in the UTLS on the radiation budget based on radiative transfer calculations by Riese et al. (2012).

To this end, we analysed measurements from three research flights of the DLR Falcon 20E and the NSF/NCAR Gulfstream ~~V~~ 5 (GV) research aircraft during the DEEPWAVE (Deep Propagating Gravity Wave Experiment) campaign in June/July 2014 above New Zealand (Fritts et al., 2016). The campaign focussed on a better understanding of the life cycle of gravity waves from excitation and propagation to dissipation at high altitudes. For the first time, DEEPWAVE combined ground-based and airborne measurements as well as satellite observations over New Zealand and the Southern Pacific – a "hotspot" region for gravity waves during the southern hemispheric winter. Here, we show results from measurements on 4 July 2014 taken during a strong mountain wave event over the Southern Alps.

First, we describe the in-situ measurements on the DLR Falcon and NSF/NCAR GV and the methods to investigate the water vapor transport induced by the mountain waves. Next, we present results for the vertical water vapor flux on a specific flight leg in the upper troposphere. Corresponding wavelet spectra reveal the location and scales of the vertical fluxes. This is followed by a general discussion of the fluxes over a wide altitude range. We then use dropsonde data to identify turbulence layers and investigate tracer-tracer correlations to quantify mixing along the flight tracks over the mountains. Finally, we discuss the effects of the mountain waves on the water vapor distribution in the UTLS and on atmospheric radiative transfer.

2 Instrumentation

During the DEEPWAVE campaign, the Falcon and the GV were equipped with a set of in-situ instruments to determine the trace gas composition and meteorological parameters. Here, we describe the instruments with relevance to this work.

2.1 Frost point hygrometer on the Falcon

The gas phase water vapor mixing ratio was determined with the cryogenic frost point hygrometer CR-2 (Buck Research Instruments, LLC) (Voigt et al., 2010; 2011). The instrument measures the temperature of a mirror covered with a thin frost

layer that is kept in thermal equilibrium with the ambient water vapor in a closed cell. An optical detector determines the thickness of the frost layer by measuring its reflectivity. The mirror is temperature-regulated so that the condensate layer thickness remains constant. In that state the mirror temperature equals the ambient frost/dew point temperature. Then, the water vapor mixing ratio can be calculated using the inverse Clausius-Clapeyron equation. The instrument covers a wide measurement range between 1 and 20,000 ppmv suitable for tropospheric and stratospheric conditions. The sampling time of the CR-2 hygrometer is 0.3 Hz. The data are quality checked by calibrations before and after the campaign against a reference MBW 373LX dew point mirror. During previous campaigns (Voigt et al., 2010; Voigt et al., 2014), the instrument agreed well (within ±10 %) with high accuracy water vapor data measured with the airborne mass spectrometer AIMS-H_2O (Kaufmann et al., 2014; 2016). For this campaign, an additional correction for low water vapor mixing ratios has been derived from simultaneous water vapor measurements on the GV research aircraft. The uncertainty of the water vapor mixing ratios is determined by systematic errors in the temperature measurements of the mirror and by the calibration accuracy. The uncertainty is 9 to 12 % for water vapor mixing ratios between 10 and 500 ppmv (Table 1). In the troposphere, the response time of the CR-2 to sudden changes in the mixing ratio is on the order of one to a few seconds. In the stratosphere, the absolute change in water vapor mixing ratios is smaller but the response time can be longer because the time to equilibrate the mirror temperature is longer for low mixing ratios. Therefore, the amplitudes in the CR-2 water vapor measurements in the stratosphere (<10 ppmv) may be damped and thus these data are not used quantitatively in this study.

2.2 Ozone measurements on the Falcon

Ozone was measured by an ultraviolet (UV) photometric gas analyser TE49 (Thermo Environmental Instruments, Inc.) (Schumann et al., 2011; Huntrieser et al., 2016). The absorbance at the wavelength of 254 nm is directly related to the ozone concentration by the Beer-Lambert law. The sampled air is split into two gas streams which flow to separate optical measurement cells. The gas in one cell serves as reference after ozone is removed by a scrubber. The two cells allow for a simultaneous measurement of both gas streams. The flow to the cells is alternated every 4 s using a selenoid valve. The response time is 15 s with a lag time of 10 s. The precision and accuracy are 1 ppbv and ±5 %, respectively.

2.3 Meteorological parameters on the Falcon

The DLR Falcon aircraft carried a basic meteorological instrumentation suite (Krautstrunk & Giez, 2012). Sensors for pressure and ~~wind~~ airflow parameters are located ~~at the~~on a noseboom in order to minimize the aircraft aerodynamic influence on the ambient air measurement.~~to realise undisturbed measurements of the ambient air.~~ Total Air Temperature (TAT) was ~~measured with~~determined using an open wire PT100 sensor located at the bottom fuselage in the front. To obtain the true static air temperature the measured TAT has to be corrected ~~by~~using the Mach number dependent correction factor~~of the aircraft~~. The measurement uncertainty is ±0.5 K. ~~The wind speed is derived by a differential pressure sensor in combination with GPS data for aircraft position and orientation.~~The three dimensional wind speed is calculated from the difference of the ground speed and the true air speed (Mallaun et al., 2015). The prior information comes from the inertial reference system and the latter is

measured with a boom mounted Rosemount 5-hole gust probe. For the horizontal wind components the measurement uncertainties are ±0.7 m s^{-1} (along wind component) and ±0.9 m s^{-1} (cross wind component) and for vertical wind ±0.3 m s^{-1}. ~~Flight altitudes are determined by a barometer as part of the inertial reference system as well as by GPS tracking. All measurements are stored with a time resolution of 1 Hz.~~An onboard GPS system is used to determine the geometric altitude while the pressure height is measured by the static pressure sensor of the 5-hole gust probe. For our analysis we use 1 Hz averages of the measurement data.

2.4 The laser hygrometer and dropsonde measurements on the GV

The NSF/NCAR GV aircraft was also equipped with instrumentation to obtain the meteorological parameters at 1 Hz time rate (Fritts et al., 2016; Smith et al., 2016). Water vapor measurements were made by an open path Vertical Cavity Surface Emitting Laser hygrometer (VCSEL, Southwest Sciences, Inc.) (Zondlo et al., 2010). The instrument was installed on the bottom fuselage of the aircraft. Two water vapor absorption lines are used to cover a wide measurement range of high mixing ratios (1853.3 nm) and moderate to low mixing ratios (1854.0 nm). The uncertainty is ±5 % at a sampling rate of 25 Hz.

On 4 July, 16 dropsondes were launched by a fully automated Airborne Vertical Atmospheric Profiling System (AVAPS) (Young et al., 2014). The dropsondes (Vaisala, Inc.) contain sensors to measure atmospheric temperature, pressure and humidity and a GPS receiver to derive winds. The data were stored at 2 Hz which provides a vertical resolution of less than 10 m in the atmosphere. The uncertainties for the temperature are ±0.2 K and for the horizontal winds ±0.5 m s^{-1}.

3 Methods

We present a novel combination of methods to analyse trace gas transport induced by mountain waves. First, we calculate the vertical water vapor flux $\overline{w'q'}$ in the measurement region as a general transport parameter correlated to the vertical wind motion. Further, the wavelet analysis of $\overline{w'q'}$ reveals the location, the wavelength and the direction of the vertical trace gas transport. Generally, the method can be applied to any conservative tracer with a gradient in the troposphere and/or the stratosphere. Thus, we apply it in this study to a flight in (nearly) cloud-free conditions. Finally, we investigate the reversibility of the transport using dropsonde data and tracer-tracer correlations.

3.1. Choice of case study and data preparation

On 4 July 2014, two flights were performed with the DLR Falcon (referred to as flight numbers FF04 and FF05) and one flight with the NSF/NCAR GV (flight number RF16) (Table 2). On that day, classified as intensive observation period (IOP) number 10 of the DEEPWAVE campaign, a strong mountain wave event with the highest vertical wave-induced energy fluxes during the whole campaign occurred (Fritts et al., 2016; Smith et al., 2016).

During IOP 10 a south-westerly and west-south-westerly flow over the South Island of New Zealand reached more than 40 m s^{-1} (Figure 1~~Figure 1~~a). The flight pattern of the DLR Falcon (Figure 1~~Figure 1~~) was chosen to be nearly parallel to the

main wind direction over the Southern Alps with Mt. Aspiring as highest summit. The flight legs above the mountains were flown four times during each Falcon flight to cover different altitudes and to determine the mountain wave situation below and above the tropopause. For the analysis, we define cross sections covering the whole mountain range at each altitude with neither an altitude change nor a turn of the aircraft. Mt. Aspiring (44.38°S, 168.73°E) was defined as the reference point for each flight leg (red triangle in Figure 1) and the distance to this reference point is used as x-axis scaling for the analysis.

In this study, we use all data in a 1 Hz time resolution. Therefore, we interpolated the lower frequency measurements to a one second time grid as consistent data input for a subsequent wavelet analysis. A sensitivity analysis using the coarser time resolution of the CR-2 (0.3 Hz) as base for the evaluation did not change the results. Since we are not looking at this point into the turbulent part of the wavelength spectrum, the 1 s-interpolation is sufficient.

3.2 Method to calculate the vertical water vapor flux

The calculation of a vertical trace gas flux was first described by Shapiro (1980). The basic assumption of this method is that we consider a conservative and passive tracer q without sources and sinks such that:

$$\frac{dq}{dt} = \frac{\partial q}{\partial t} + \vec{v} \cdot \overrightarrow{\mathrm{div}(q)} = 0, \tag{1}$$

Where t is the time, $\vec{v}$ is the vector field of the horizontal and vertical wind components u, v and w and $\overrightarrow{\mathrm{div}(q)}$ is the divergence of the passive tracer. Since there were no clouds over the mountain transect for the analysed altitudes, water vapor is a conservative tracer in our case and its distribution is not influenced by condensation or sublimation.

The quantity q as well as the wind components may be expressed in terms of a spatial (x) or temporal mean $\bar{q}$ and perturbations q':

$$q(x) = \bar{q} + q'(x). \tag{2}$$

Under the assumption that we can neglect the mean horizontal and vertical advection of $\bar{q}$ in the measurement region we consider the local temporal change of $\bar{q}$ as:

$$\frac{\partial \bar{q}}{\partial t} = -\frac{\partial}{\partial x}(\overline{u'q'}) - \frac{\partial}{\partial y}(\overline{v'q'}) - \frac{\partial}{\partial z}(\overline{w'q'}), \tag{3}$$

where u' and v' are the horizontal wind perturbations and w' is the vertical wind perturbation. The overbars mark the mean trace gas flux over spatial or temporal intervals. Furthermore, we assume that the horizontal flux divergences are negligible compared to the vertical flux divergence and hence eq. (3) reduces to:

$$\frac{\partial \bar{q}}{\partial t} = -\frac{\partial}{\partial z}(\overline{w'q'}). \tag{4}$$

The local vertical trace gas flux is then determined by

$$w'q'(x) = q'(x) \cdot w'(x), \tag{5}$$

where the perturbations depends on the filter function used to receive the spatial mean:

$$\bar{q} = \frac{1}{x_2 - x_1} \cdot \int_{x_1}^{x_2} q(x)dx. \tag{6}$$

We derive the mean vertical trace gas flux $\overline{w'q'}$ from integrating over selected spatial or temporal intervals along the mountain cross section (see section 4.4). For an ideal linear wave, the mean vertical flux would be zero. If we observe a negative or positive mean flux, a trace gas transport will exist but we need further analysis on the irreversibility of the transport process.

The filter function and its characteristics have an important influence on the results. We have to decide which scales of horizontal wavelength to include and which parts of the spectrum to neglect. In this study, the length of the flight legs limits the maximum resolvable horizontal wavelength to less than 150 km. In addition, a change in the wind direction in front of the mountains partially influences the water vapor distribution at wavelengths larger than 80 km. Therefore, a suitable filter choice in our case is a bandpass filter with a lower limit of 300 m and an upper limit of 80 km. It must be kept in mind that the bandpass filter as spatial filter method may damp wavelengths due to edge effects (Ehard et al., 2015). We apply the filter to the water vapor measurements as well as to the vertical wind measurements.

3.3 Wavelet analysis method

Wavelet analysis is widely used in gravity wave analysis to identify the location and wavelength scale of waves (e.g. Woods & Smith, 2010; Placke et al., 2013; Zhang et al., 2015). By combining power spectra and cospectra of the variables of interest, flux carrying waves can be characterized. We calculated normalized power spectra of the vertical wind and the water vapor perturbation using the Morlet wavelet as defined in Torrence & Compo (1998) and an equalized distance of 200 m between each data point. For the calculation we create standard normal distributed perturbed variables q' and w'.

The cospectrum $W_n^{XY}(s)$ of the vertical ~~water vapor~~trace gas flux ~~$w'H_2O'w'q'$ $(q' = H_2O')$~~ combines the real parts of the wavelet spectra of both variables:

$$W_n^{XY}(s) = \Re\{W_n^X(s)W_n^{Y^*}(s)\}, \tag{7}$$

where X and Y represent the variables w and ~~H_2Oq~~, n classifies the localised position index, s is the wavelet scale and * is the complex conjugate. This results in the in-phase contributions to a product from different wavelengths. The significance is determined with the method from Portele et al. (2017) as follows:

$$\frac{|W_n^X(s)W_n^{Y^*}(s)|}{\sqrt{|P_k^X P_k^Y|}} = \frac{\chi_\nu^2(p)}{\nu}, \tag{8}$$

where P_k represents the normalized Markov red noise spectrum with the frequency index $k = 0 \dots N-1$ with N as the number of points in the data series, χ_ν^2 is the chi-square distribution for ν degrees of freedom and p is the significance. For this case we use in eq. (8):

$$P_k = \frac{1-\alpha^2}{1+\alpha^2-1\alpha\, cos(2\pi k/N)}, \tag{9}$$

a combined autocorrelation factor α with a lag of one and a lag of ten ($\alpha = lag1 + \sqrt{lag10}/2$). The original time series is correlated with a delayed copy of itself (time lag) to obtain the significant parts of the cospectrum. The chosen combination includes signals of larger wavelengths (significant for high time lags) and smaller wavelengths (significant for lower lags)

without stressing any of them ~~that gives defined significant areas with uniform weighting of low and high fluxes over the wavelength scale~~ (Portele et al., 2017).

4 Results

First, we show the results of the flux calculations and wavelet analysis for one selected flight altitude. Then, we discuss the water vapor measurements on different flight altitudes to characterize the vertical flux from the upper troposphere to the lower stratosphere. Finally, we use dropsonde data to identify regions with enhanced turbulence and with a vertical gradient of the potential temperature close to zero. Additionally, we investigate mixing processes in the measurement region using tracer-tracer correlations, in this case of water vapor and ozone.

4.1 Synoptic situation on 4 July 2014

Mesoscale simulations with the Weather Research and Forecasting (WRF) model, version 3.7 (Skamarock et al., 2008) were performed to give an overview of the synoptic situation. Two nested domains with horizontal resolutions of 6 km and 2 km and 138 vertical levels with a model top at 2 hPa were used. The model is initialized with operational analyses of the ECMWF model at 18 UTC on 3 July 2014 and run for 36 hours. A detailed overview of the same model set-up including the parameterizations used can be found in Ehard et al. (2016) for a gravity wave event over northern Scandinavia.

For 4 July 2014 the orographic forcing over the Southern Alps was induced by a south-westerly wind of ~20 m s^{-1} at 850 hPa at the west coast of the South Island of New Zealand (not shown). Up to the tropospheric jet level around 8.9 km (at 300 hPa), horizontal wind speeds in the upstream region accelerate up to 50 m s^{-1} (Figure 1~~Figure 1~~a). Over the mountains the horizontal wind velocities decreased to 30 to 40 m s^{-1} (Figure 1~~Figure 1~~b) and changed from a westerly direction west of the South Island to south-westerly. A part of the core region of the tropospheric jet was located west of the South Island (Figure 1~~Figure 1~~b). The strong low-level flow forced mountain waves as clearly indicated by the vertical wind speed values over the island at 8.9 km altitude (Figure 1~~Figure 1~~c). The mountain waves are excited in the lower troposphere and propagate vertically through the tropopause region and lower stratosphere (Figure 1d).

The intensity of the mountain wave forcing over New Zealand on 4 July 2014 changed within several hours. The forcing at the west edge of the mountains was strongest at 06 UTC and weakened till 18 UTC. Also, a low pressure system south of New Zealand moved quickly eastward and led to a thermal tropopause (WMO, 1957) descending from 11.1 km to 9.5 km during the observation period. A detailed overview of the synoptic situation for 4 July 2014 is given by Bramberger et al. (2017).

4.2 Vertical water vapor flux at 8.9 km

An overview of the first Falcon flight FF04 on 4 July 2014 is shown in Figure 2. We identify strong fluctuations in water vapor, potential temperature and horizontal and vertical wind components at different altitudes during the flight. In particular, the vertical wind component varied ±5 m s^{-1} over the mountains (bottom panel). For water vapor we detect the strongest

perturbations in the same region over the mountains during the first and second flight leg (7.7 and 8.9 km) with amplitudes of up to 100 ppmv. The amplitudes decrease with altitude due to the general decline of the H_2O concentrations in the UTLS. Ozone shows strong variations over the mountains in the stratosphere and less variability in the troposphere, opposite to the H_2O signal. Also, the potential temperature as well as the horizontal wind components displays fluctuations above the mountains. The location and extent of the fluctuations imply mountain waves as source as suggested by studies from Smith et al. (2016) and Bramberger et al. (2017).

For this work we chose the second flight leg at 8.9 km as an example to analyse the water vapor transport (Figure 3). In the upper troposphere the water vapor measurements with the CR-2 hygrometer are very sensitive to sudden changes in the mixing ratio as caused by mountain waves. The flight leg is located in the upper troposphere with a distance of approximately 2 km to the thermal tropopause at 10.9 km. The wave signature in water vapor is very distinctive with high amplitudes of 20 ppmv above the Mt. Aspiring transect. The potential temperature shows a similar wave pattern as water vapor, but anti-correlated (selected instances indicated by vertical blue dashed lines in Figure 3) and following the vertical wind fluctuations. Additionally, there is a slow decrease in the water vapor mixing ratio from -80 km distance to the summit at $x = 0$ km, along with an increase in the potential temperature of 3 K and a change in the wind direction. The upstream region of the transect is located in the vicinity of the tropospheric jet stream which may influence the upstream water vapor distribution by horizontal larger-scale processes.

Results from the flux calculations for this flight leg are displayed in Figure 4. We applied the bandpass filter with an upper limit of 80 km wavelength to the water vapor and the vertical wind data and show the received perturbations w' and H_2O' in panel (a). The two variables are 90° phase shifted with respect to each other which can be also observed by the diagonal blue dashed lines in the bottom panel of Figure 3. This phase shift is caused by a direct response of water vapor to the vertical wind motion. We assume an atmosphere finely layered with conserved quantities. These layers are disturbed by propagating gravity waves and an aircraft flying at a constant level penetrates the layers repeatedly as depicted in Figure 10 of Smith et al. (2008). At a constant altitude therefore the trace gas concentration and potential temperature follow the vertical wind variations with a phase shift of 90°.

A strong wave signature is detected in the local vertical water vapor flux $w'H_2O'$ above the mountains (Figure 4b). The vertical flux is very small in the upstream region and the amplitude increases over the mountains from west to east. Figure 4c shows the integrated vertical water vapor flux. It is generally ~~positive~~ increasing above the mountains between +30 and +60 km and from +90 to +180 km distance to the Mt. Aspiring summit with a maximum of 39,000 $m^2 s^{-1}$ ppmv and 76,000 $m^2 s^{-1}$ ppmv, respectively. Further east we find a negative trend (-98,000 $m^2 s^{-1}$ ppmv)~~(-176 m ppmv)~~ induced by little water vapor perturbations but enhanced vertical wind fluctuations. At the western edge of the mountains (between -50 and +30 km) we also observe a negative flux. This region is located in the vicinity of the tropospheric jet stream which influences the distribution of the water vapor mixing ratio by horizontal transport processes (Figure 3: decrease of H_2O from West to East between -80 km and 0 km distance). This behavior cannot fully be eliminated by the used filter and is thus present in the water vapor perturbations by a few fluctuations with a negative weighting.

Since water vapor has a negative gradient in the troposphere, a positive flux mainly indicates upward transport of high mixing ratios to a level of lower mixing ratio. A negative flux points to a downward transport. Thus, we find a strong indication of an integrated upward water vapor flux above the Southern Alps and a downward flux above the eastern part of the mountains for this flight leg.

For the flux calculations we ~~defined~~ used water vapor as conservative tracer due to the absence of supersaturation at the analysed flight altitudes. However, at the first flight leg of FF04 at 7.7 km we measured ice particles with the in-situ instrumentation with a detection limit for the ice water content of 0.2 ppmv. The cloud was detected between +150 km and +200 km distance ~~that~~and indicates the existence of a lee wave cirrus. ~~These~~ This gravity wave induced clouds ~~were~~was also visible in the infra-red images of the MTSAT-2 satellite at 03 UTC and dissipated until 06 UTC (Bramberger et al., 2017). No further clouds were measured on the other flight legs and in particular not during those legs for which the flux calculations were performed. However, the presence of an ice cloud on a lower layer ~~This~~ may affect the water vapor distribution at ~~the next~~a higher flight level ~~at (~~8.9 km) by lowering the amplitude of the fluctuation. In Figure 3 we observe a strong negative peak in the vertical wind at +170 km distance to the summit in contrast to a small water vapor fluctuation which may be influenced by the drying of the level below. The calculated flux in this region is then also reduced. This effect does not influence the general transport direction at this flight altitude and is not relevant for the higher flight altitudes or the second Falcon flight since these lee wave clouds were not observed above 7.7 km and dissipated during the first flight.

4.3 Wavelength spectrum of the vertical water vapor flux

Wavelet analysis is used to quantify location, scale and direction of the vertical water vapor flux. Figure 5 shows the amplitudes of perturbations in vertical wind (a) and water vapor (b) for the second flight leg of FF04 for horizontal wavelengths between 300 m and 400 km. The power spectra represent the variance wavelets for w' and H_2O' while the cospectrum shows the covariance wavelet for $w'H_2O'$. Highest activity in both variables occurs for wavelengths between 10 km and 80 km, where the upper limit results from the bandpass filter. Moreover, the peaks are located above the middle and eastern part of the mountains. We find similar patterns in w' and H_2O' but of different intensity. Water vapor has the strongest peak at +75 km distance and at 22 km horizontal wavelength, whereas the intensities of the vertical wind perturbation are strongest further east at +180 km from the summit with a broader wavelength range between 15 and 30 km. The power of the water vapor fluctuation in this region may be reduced due to condensation at the flight altitude below as mentioned before. Since the flight legs are short in the downstream region, data for $x >$ +200 km lie in the cone of influence (COI) area and thus require careful interpretation due to edge effects of the analysis (Torrence & Compo, 1998). Additionally, we find a layer of enhanced magnitude in the power of the water vapor perturbations at a wavelength of about 60 km located at -80 to +100 km distance. This may be caused by longer waves that are not part of this analysis and that are influenced by horizontal advection due to the tropospheric jet stream. There are some significant areas in the upstream region as well as over the eastern part of the mountains in both power spectra for wavelengths ~~<~~larger than 10 km with amplitudes ~~<~~smaller than 0.1 m^2 s^{-2} and ~~<~~smaller than 0.1 $ppmv^2$, respectively. This indicates additional small scale fluctuations in the parameters that may not be relevant for

transport of water vapor but for mixing processes. These small scale fluctuations are especially observed for the vertical wind over the middle and eastern mountain region at the higher altitudes (not shown) where we find indications for turbulence in the dropsonde data (see section 5).

In the right panels of Figure 5, we show the global wavelet spectrum (GWS) where the power is averaged over all local wavelet spectra. This highlights the dominant wavelengths along the flight path. Most power is carried in wavelengths smaller than 30 km for both variables. A second mode with less power is found between 40 and 80 km horizontal wavelength.

Figure 5c shows the corresponding cospectrum of $w'H_2O'$. As in the individual power spectra we identify dominant horizontal wavelengths between 10 and 80 km. The location of upward or downward transport is represented in the colour-coding with red areas indicating an upward H_2O flux and blue the opposite. The significant parts from the individual power spectra contribute to the local flux. Horizontal wavelengths between 22 and 60 km dominantly contribute to an upward water vapor transport above the mountain region. The downward water vapor flux above the eastern mountain part is mainly carried by wavelengths between 20 and 22 km. The vertical wind perturbation dominantly influences this transport direction. Quadrant analysis of w' and H_2O' (not shown) reveal that the positive flux $w'H_2O'$ is dominated by the upward transport of high humidity in regions with low humidity for wavelengths larger than 22 km. Less pronounced is the downward transport of low humidity that also cause a positive flux. The negative flux for horizontal wavelengths smaller than 22 km is a result of the upward transport of low humidity and the downward transport of high humidity in equal parts which caused a reduced water vapor mixing ratio in this region.

The results show an overall upward transport of H_2O at this flight altitude. Further, a superposition of wave packets with different characteristics is detected in the mountain wave region. The rugged terrain of the Southern Alps with many crests and valleys may initiate these different contributions to the full spectrum. In the statistical analysis of all GV flight level data during DEEPWAVE, Smith et al. (2016) also observed small and longer scale waves with different characteristics. In their study flux-carrying waves are larger than 20 km horizontal wavelength. Small scale waves with wavelengths around 20 km and less are mainly dominating in the vertical wind motion and do not carry any energy or momentum flux upward (Smith & Kruse, 2017). This is explained by dynamic reasons since only the longer-scale waves that propagate vertically and are not evanescent transport energy and momentum vertically. For water vapor as passive tracer the reasons for the chosen scale separation are the same in this wavelength range. Transport processes by large-scale waves with horizontal wavelengths larger than 100 km would be presumably different for energy or momentum and water vapor.

4.4 Vertical profile of the water vapor flux from the troposphere to the stratosphere

We combine GV and Falcon data on 4 July 2014 to derive a profile of the vertical water vapor flux in the UTLS region. The Falcon flights FF04 and FF05 covered a temporal evolution of the mountain wave activity that increased from the first to the second flight (Bramberger et al., 2017). The GV operated simultaneously to the second Falcon flight FF05 (Table 2). Both aircraft flew on the same flight track but at different altitudes to measure the vertical propagation of the mountain waves. In Figure 6a, we show the Falcon flight legs 1 to 3 (FF05) between 7.7 and 10.8 km and two GV flight legs at 12.0 and 13.0 km

that took place at the same time as leg 3 and leg 4 of FF05. The fourth leg of FF05 is not shown since amplitudes in the water vapor fluctuations cannot be fully resolved by the CR-2 in the stratosphere. During all Falcon and GV transects, we find significant water vapor fluxes over the mountain region (Figure 6a). The thermal tropopause was located at about 10.5 km, thus the observed water vapor flux extends above the tropopause. The wave pattern remains nearly stationary through all altitudes with, for example, a strong wave package at about +110 km distance from the reference point. Upstream and downstream regions exhibit very low or no vertical fluxes.

To derive a vertical profile of the vertical water vapor flux in the mountain wave region, we define a range between the highest summit (x = 0 km) and the east end of the Southern Alps (x = 202 km). For this region, the integrated vertical water vapor flux is normalized by the length. The results at each altitude are plotted in Figure 6b. To distinguish the transport characteristics of different horizontal wavelengths, we show the profile for wavelengths between 300 m and 80 km and between 22 km and 80 km, respectively. Under the assumption of quasi-stationary mountain waves, we neglect the time shift (~3 h) between the single flight legs.

In general, a negative (positive) flux divergence $\frac{\partial(\overline{w'H_2O'})}{\partial z}$ humidifies (dries) the layer above due to the negative water vapor gradient in the atmosphere. By the absence of vertical or horizontal transport and the existence of a well-mixed atmosphere, ~~we are expecting~~ no flux divergence is expected. In the mountain region we see positive flux divergences in the troposphere (7.7 – 8.9 km) and lower stratosphere (10.8 – 12.0 km) for horizontal wavelengths between 300 m and 80 km (Figure 6b) which may indicate a general downward transport (Table 3). The strong negative vertical flux at the lowest altitude may be influenced by transport and mixing processes that lie below this level and that are not covered by the in-situ measurements. This may be convective processes in front or over the mountains. The positive flux divergence in the layer from 10.8 to 12 km implies a drying of the atmosphere by a downward transport. In the layer below, from 8.9 to 10.8 km, a strong upward transport from the upper troposphere through the tropopause occurs which is indicated by the negative flux divergence. This process may lead to the observed enhanced water vapor mixing ratios at around 10.8 km and below (see section 6). Since we only have measurements on a few defined altitudes an exact localisation of maxima and of sign changes of the transport direction is not possible. For the first Falcon flight we find a similar pattern and values for the flux divergence between 7.7 and 10.8 km (Table 3). The use of other levels could change the pattern slightly but the general trend appears to be robust. Vertically resolved data (e.g. by lidar measurements) would be required to derive the vertical curtain of the flux divergence but were not performed during this campaign.

The picture changes when excluding the small wavelengths below 22 km (dashed line in Figure 6b). We then find a negative flux divergence over the broad altitude range from upper troposphere to lower stratosphere (8.9 – 13 km). This indicates a dominating upward transport of water vapor by the larger wavelengths (see Figure 5c). When comparing both profiles, the difference between them in the layer between 8.9 and 12.0 km suggests that the positive flux divergence (downward transport) between 10.8 and 12.0 km is mainly induced by small horizontal wavelengths (Table 3). These smaller wavelengths indicate

instabilities in the atmosphere and thus the upward mountain wave propagation may be influenced by local turbulence (see section 5) or by downward propagating gravity waves that are excited aloft (Bramberger et al., 2017).

5 Turbulence in the UTLS region

Gravity waves may cause or enhance turbulence by instabilities, wave breaking, and dissipation (e.g. Pavelin et al., 2002; Fritts & Alexander, 2003; Whiteway et al., 2003). Here, we use dropsonde launches from the GV to investigate turbulence potentially induced by the mountain waves which may cause mixing of trace species in the measurement region. Therefore, we calculate potential temperature and Richardson numbers (Ri) from the data set. In general, a Richardson number below 0.25 indicates an unstable flow that initiates turbulence (Miles, 1961; Howard, 2006). Further, there is evidence that turbulence is maintained for Ri <1.0 after being initiated (e.g. Woods, 1969; Müllemann et al., 2003). Regarding potential temperatures, it is interesting to identify regions with a vertical gradient close to zero ($\frac{\partial \theta}{\partial z} \rightarrow 0$) since this indicates mixing over a specific altitude range.

During flight RF16, 15 dropsondes were launched in the near upstream region at the west edge of the mountains, above and at the east side of the mountains. Example profiles of temperature and wind measurements and the derived potential temperature and Richardson number of one dropsonde launched at 07:55 UTC (during FF05) are shown in Figure 7a. The position of the launch above the Southern Alps at +69 km distance (44.39°S, 169.60°E) is marked in Figure 1~~Figure 1~~ with a red dot. The thermal tropopause is found at an altitude of 10.6 km which is consistent with the WRF model calculations and is shown by the horizontal red dotted line in Figure 7a. In the vicinity of the thermal tropopause we find a strong vertical shear of the horizontal wind (approximately 0.02 s^{-1}) induced by the tropospheric jet stream whose core region is located west of the Southern Island. In this region of vertical wind shear Ri decreases below the critical level value of 0.25 indicating dynamic instabilities and local turbulence (Pavelin et al., 2001; 2002). Simultaneously, the gradient in the potential temperature is strongly attenuated. For altitudes below 9.2 km, layers with Ri <1.0 exist which may be evidence for further turbulence or static instabilities. In the altitude range between 9.2 and 10.2 km Ri is clearly larger than 1.0 and the potential temperature profile shows an enhanced gradient.

In Figure 7b profiles of potential temperature and Ri of two dropsondes that were launched at the same location over the Southern Alps (Figure 1~~Figure 1~~) at 06:52 and 11:37 UTC show the temporal evolution over the course of the IOP. Within 5 hours the thermal tropopause descended from 11.1 km to 10.4 km. The potential temperature of the dropsonde at 11:37 UTC shows many layers with a small gradient caused by mixing processes which occurred earlier during the event. In general, the Richardson number increased in the UTLS but still shows some evidence for turbulence (Ri <1.0) right below the tropopause. At the same time the vertical shear of the horizontal winds declined (not shown) which agrees with the weakening of the gravity wave event.

The layers of suggested turbulence~~.~~, found in all nine dropsondes launched above the middle and eastern part of the mountains, generally have a thickness of approximately 200 m and are correlated with a potential temperature range of 329 to 334 K. The

gradient of the potential temperature in these layers is less than 5 K km^{-1}. This low gradient may be a result of initiated mixing of air masses by local turbulence.

Upstream of the mountains, wind shear regions and dynamic instabilities are not as obvious as over the middle and eastern mountains (not shown) indicating that this feature is mainly caused by the mountain waves.

Another characteristic factor is the Scorer parameter ℓ that is shown in Figure 7c for the dropsonde launched at 07:55 UTC (44.39°S, 169.60°E) The Scorer parameter is used to estimate the critical horizontal wavelengths allowing vertical propagation of linear gravity waves under the given atmospheric conditions. The vertical profile of ℓ shows that gravity waves with horizontal wavelengths between 10 and 20 km are able to propagate vertically if they are excited in the lower troposphere. Between 4 and 9 km altitude, wave modes with horizontal wavelengths smaller than the critical wavelength of about 22 km become evanescent and may be attenuated. The magnitude of the estimated critical wavelength based on the Scorer parameter confirms our observations in the power spectra and wavelet cospectrum (Figure 5): the upward transport of water vapor is dominated by horizontal wavelengths larger than 22 km. A downward transport is possible by wavelengths smaller than 22 km due to a wave attenuation in the upper troposphere that is responsible for damping and partial reflecting of gravity waves. The vertical profile of ℓ is similar for all dropsonde launches (upstream and over the mountains) and is also comparable to an upstream ℓ-profile from the IFS forecast shown in Figure 3b in Bramberger et al. (2017).

6 Mixing identified by tracer-tracer correlation

Tracer-tracer correlations are widely used to investigate mixing of trace gases and thus can support our findings presented in the previous sections. We use the correlation between water vapor and ozone, where water vapor has a strong negative gradient in the troposphere and ozone a strong positive gradient in the lower stratosphere. In Figure 8 we show the H_2O-O_3 correlation of an unperturbed non-gravity wave Falcon flight (FF03 on 2 July 2014) and of the gravity wave flights FF04/FF05 on 4 July 2014. The flight pattern of FF03, the only flight under non-gravity wave conditions in the UTLS throughout the campaign, is similar to the gravity-wave flights, with four transects over the Southern Alps at different altitudes.

The H_2O-O_3 correlation in unperturbed conditions (grey dots) shows a clear L-shape indicating very little or no mixing of air masses. In contrast, the H_2O-O_3 correlation in the UTLS region on 4 July deviates from the L-shape. This indicates mixing in the tropopause region most likely related to the mountain waves as shown in the previous section. The mixing is strong at potential temperatures between 329 and 334 K in the UTLS region as identified by local turbulence in the dropsonde data. The dropsondes, covering a time range of 5 hours before, during and after the second Falcon flight FF05, always show turbulence in the same potential temperature range with slight changes in the altitude due to the descent of the thermal tropopause. Thus, we also assume the presence of turbulence layers for similar potential temperatures during the first Falcon flight FF04. This potential temperature range is marked in the ozone measurements at 10.8 km altitude for flight FF04 over the middle and eastern part of the mountains (Figure 8b, inlay) where we also observed the highest mountain wave activity (section 4.3). Furthermore, we suggested in section 4.4 enhanced mixing ratios at this altitude by the shape of the vertical profile. By looking

into the data in the mixing region (60 – 160 ppbv O_3 and 8 – 11 ppmv H_2O) in Figure 8b, we also find data points beyond the defined potential temperature range for mixing (329 – 334 K) (green dots). These data are located over the upstream region on the flown transect. They are not following the ideal L-shape for no mixing but have less enhanced water vapor mixing ratios than the mixed data points (red dots). The same observation is found for flight FF05 at 10.8 km altitude but for higher ozone and lower water vapor mixing ratios since the tropopause was located at a lower altitude. Furthermore, we suggest local turbulence and induced mixing over the mountain region also for the first Falcon flight due to a similar mountain wave activity.

While the pure kinetic transport of water vapor by waves might in general be reversible, mixing implies a permanent change in the water vapor distribution in the UTLS region. The combined analysis of in-situ aircraft measurements and dropsonde data shows a transport of water vapor through the upper troposphere and lower stratosphere and a partial mixing of the air masses caused by mountain waves.

7 Effect on the atmospheric radiation budget

The water vapor mixing ratio in the UTLS strongly influences the radiative transfer in this region. Here, we try to derive an estimate of the radiative forcing by the enhanced water vapor mixing ratios in the UTLS caused by the mountain waves based on simulations by Riese et al. (2012). They studied the influence of uncertainties in the atmospheric mixing strength on global UTLS distributions and the associated radiative effects of water vapor and other trace species. To this end, Riese et al. (2012) used multiannual simulations with the Chemical Lagrangian Model of the Stratosphere CLaMS (McKenna et al., 2002a; McKenna et al., 2002b). In their Figure 6, Riese et al. (2012) show the radiative effects at the top of the atmosphere of a certain change in water vapor mixing ratios for the year 2003. For our flight conditions (approximately 300 hPa) and location (New Zealand, -45° latitude), a 10 % increase in water vapor mixing ratios near the tropopause results in a radiative forcing of 0.5 to 1 W m^{-2}. The percentage change between the reference and the enhanced mixing case is derived from Figure ~~6~~5 in Riese et al. (2012). For our case, from the water vapor to ozone correlation we assume a minimum increase of 4 ppmv (~30 %) ~~*H*~~*2O* ~~-~~ H_2O in the mixed mountain wave region (red dots in Figure 8b) with respect to the less influenced upstream region (green dots). Under the assumption that the simulated difference in the distribution of water vapor as a result of enhanced mixing may also be representative for our case of mixing induced by mountain waves, we estimate a radiative forcing larger than ~~Under the assumption that the change in the climatological distributions of water vapor may also be representative for our case of mixing induced by mountain waves, we estimate a radiative forcing ≥~~1 W m^{-2} locally above New Zealand during and after the mountain wave event. Riese et al. (2012) do not give a physical reason for the changes in the mixing strength, so our case may present a physical process (among other processes) contributing to the change in the water vapor distribution in the UTLS. While we used the calculations by Riese et al. (2012) at the measurement location, their study has a coarser vertical and horizontal resolution and is averaged over one year. We here neglect the seasonality in the water vapor mixing ratio that is present in the southern hemisphere at this latitude range. Thus, our estimate has a large uncertainty. Nevertheless, it

emphasizes the relevance of mountain waves on the water vapor distribution and the radiation budget of the UTLS. An upper estimate of the radiative forcing for this case may be determined by the difference between the unperturbed conditions in flight FF03 and the mixed conditions in flights FF04/FF05. The increase in water vapor mixing ratio of ~11 ppmv (160 %) may result in a significantly larger local radiative forcing. While the analysis of Riese et al. (2012) reflects the impact of uncertainty in the atmospheric mixing strength in the UTLS region on a global and multiannual scale, we use it here to derive a rough estimate of the local radiative effects of mountain waves for a short time period (few hours to one day). Further studies are required to evaluate the radiative forcing caused by changes in the water vapor mixing ratios due to gravity waves in more detail ~~and/or on larger scales~~. However, our crude estimate shows that mountain waves have a great potential to change the water vapor distribution of the UTLS with significant effects on climate.

8 Conclusion and outlook

Based on in-situ aircraft measurements of water vapor and wind during the DEEPWAVE campaign we combined selected methods to investigate the vertical transport of water vapor induced by mountain waves. Flux calculations showed regions with enhanced mountain wave activity above the Southern Alps on 4 July 2014. While the meteorology of this day and the propagation of the observed mountain waves is also discussed in Bramberger et al. (2017) and Smith et al. (2016), we concentrated on the effect of the mountain wave activity on the water vapor distribution in the UTLS. Stimulated by the flux calculation method by Shapiro (1980) and Schilling et al. (1999), we, for the first time, used in this study water vapor as a transport tracer in a wide altitude range throughout the UTLS.

Significant vertical water vapor fluxes observed by the Falcon and the GV at different flight altitudes below and above the tropopause indicated mountain wave propagation and water vapor transport through the tropopause. Forced by a strong south-westerly wind, the mountain wave activity was highest in the middle and eastern part over the Southern Alps. A wavelet analysis helped to identify the location, the direction, and the horizontal wavelength scale of the observed transport process. Covering the wavelength range of 300 m to 80 km we found an upward transport of water vapor above the mountains at horizontal wavelengths between 22 and 60 km at 8.9 km flight altitude. Further east a downward transport at smaller wavelengths <22 km occurred. Thus, the water vapor transport happened at the same horizontal wavelengths as the energy and momentum transport for this case (Smith et al., 2016). The vertical profile of the Scorer parameter determined from dropsonde launches confirms a vertical propagation of horizontal wavelengths between larger than 10 km. However, wavelengths smaller than the critical wavelength of about 20 km may be damped and partial reflected in the upper troposphere.

The vertical flux divergence over the mountains within the altitude range 8.9 to 13.0 km suggests dominating upward water vapor transport through the tropopause with enhanced mixing ratios at around 10.8 km altitude and below. A downward transport in the layer between 10.8 and 12 km occurred for horizontal wavelengths <22 km and may be related to turbulence we observed in the dropsonde data. While Smith et al. (2016) and Smith & Kruse (2017) showed that there is no energy and momentum flux for these small-scale waves, we observed that a mass transport of water vapor occurred in small scales. This

may point to more complex transport mechanisms of trace gases in mountain waves. To obtain the vertical water vapor flux we neglected horizontal and vertical advection in the measurement region but there were hints for additional transport processes such as convection or advection induced by the tropospheric jet stream, especially in the upstream region. These processes may also influence the measurements above the Southern Alps but they should be dominated by the vertical transport induced by the mountain waves. The occurrence of lee wave clouds at the lowest flight altitude (7.7 km) during a short time period of the first Falcon flight may additionally influence the vertical water vapor flux at 8.9 km by reducing ~~it~~its magnitude in the eastern part of the mountains. Since there is a time shift between the measurements at both altitudes and a vertical layer of more than 1 km between them without cloud observations, we cannot quantify the effect in this study.

In addition we investigated mixing processes induced by the mountain waves. We found indications for turbulence in dropsonde data collected over the mountain transect. Wind shear, located near and below the thermal tropopause, resulted in Richardson numbers <1.0 relevant for turbulence. We detected enhanced turbulence over few hours related to high mountain wave activity which induced mixing of water vapor in the upper troposphere over the Southern Alps. In addition the H_2O-O_3 ~~$H_2O - O_3$~~ correlation showed enhanced mixing for the mountain wave situation compared to unperturbed conditions. Thus, we explain the water vapor distribution in the UTLS for this case by a combination of vertical transport of water vapor and mixing, both related to the observed mountain waves.

The enhanced water vapor mixing ratios in the tropopause region strongly influences the radiative transfer in the UTLS. The estimated~~locally and temporally limited~~ radiative forcing for our case, locally and temporally limited over the Southern Alps of New Zealand, exceeded 1 W m^{-2} and suggests that mountain waves occurring in many locations all over the world may have a non-negligible ~~large~~ effect on climate.

Further studies and simulations, e.g. with the Weather Research and Forecasting (WRF) model (Wagner et al., 2017), can help to enhance our understanding of the main transport and mixing processes. For example, the influence of wind shear near the tropopause and resulting small-scale turbulence may be further investigated. Regional and global modelling could help to quantify the global changes in the UTLS water vapor distribution caused by mountain waves and their effects on the atmospheric radiation budget.

Generally, the application of our novel combination of methods to a broader data set can help to better understand the mountain wave induced change in the water vapor distribution of the UTLS and their impact on the atmospheric radiation budget.

Acknowledgements

Part of this research was funded by the German research initiative "Role of the Middle Atmosphere in Climate (ROMIC/01LG1206A)" of the German Ministry of Research and Education in the project "Investigation of the life cycle of gravity waves (GW-LCYCLE)". Further the Deutsche Forschungsgemeinschaft (DFG) supported this work via the SFB MS-GWaves (GW-TP/DO 1020/9-1, PACOG/RA 1400/6-1) and the HALO-SPP 1294 (grant no. VO 1504/4-1). The U.S. research was funded by NSF and NCAR/EOL. Christiane Voigt appreciates support by the Helmholtz Association under grant no. W2/W3-60. We thank the DLR flight department for excellent support of the campaign. The observational data are available at https://halo-db.pa.op.dlr.de/ and http://data.eol.ucar.edu. Michael Lichtenstern and Monika Scheibe did the ozone measurements during the campaign. Many thanks to Prof. Peter Hoor and his group from University of Mainz for the constructive discussion about trace gas transport influenced by mountain waves. The first author also wants to thank Prof. Ron Smith for helpful hints on the data analysis and Sonja Gisinger for proofreading. We thank the anonymous referees for their helpful comments on the manuscript.

References

Bramberger, M., Dörnbrack, A., Bossert, K., Ehard, B., Fritts, D. C., Kaifler, B., Mallaun, C., Orr, A., Pautet, P. D., Rapp, M., Taylor, M. J., Vosper, S., Williams, B., and Witschas, B.: Does strong tropospheric forcing cause large-amplitude mesospheric gravity waves? - A DEEPWAVE Case Study, J. Geophys. Res. Atmos., accepted, 2017.

Danielsen, E. F., Hipskind, R. S., Starr, W. L., Vedder, J. F., Gaines, S. E., Kley, D., and Kelly, K. K.: Irreversible Transport in the Stratosphere by Internal Waves of Short Vertical Wavelength, J. Geophys. Res. Atmos., 96(D9), 17433-17452, doi:10.1029/91jd01362, 1991.

Ehard, B., Achtert, P., Dörnbrack, A., Gisinger, S., Gumbel, J., Khaplanov, M., Rapp, M., and Wagner, J.: Combination of Lidar and Model Data for Studying Deep Gravity Wave Propagation, Mon. Weather Rev., 144(1), 77-98, doi:10.1175/mwr-d-14-00405.1, 2016.

Ehard, B., Kaifler, B., Kaifler, N., and Rapp, M.: Evaluation of methods for gravity wave extraction from middle-atmospheric lidar temperature measurements, Atmos. Meas. Tech., 8(11), 4645-4655, doi:10.5194/amt-8-4645-2015, 2015.

Fischer, H., Wienhold, F. G., Hoor, P., Bujok, O., Schiller, C., Siegmund, P., Ambaum, M., Scheeren, H. A., and Lelieveld, J.: Tracer correlations in the northern high latitude lowermost stratosphere: Influence of cross-tropopause mass exchange, Geophys. Res. Lett., 27(1), 97-100, doi:10.1029/1999gl010879, 2000.

Fritts, D. C., and Alexander, M. J.: Gravity wave dynamics and effects in the middle atmosphere, Rev. Geophys., 41(1), doi:10.1029/2001rg000106, 2003.

Fritts, D. C., Smith, R. B., Taylor, M. J., Doyle, J. D., Eckermann, S. D., Dörnbrack, A., Rapp, M., Williams, B. P., Pautet, P. D., Bossert, K., Criddle, N. R., Reynolds, C. A., Reinecke, P. A., Uddstrom, M., Revell, M. J., Turner, R., Kaifler, B., Wagner, J. S., Mixa, T., Kruse, C. G., Nugent, A. D., Watson, C. D., Gisinger, S., Smith, S. M., Lieberman, R. S.,

Laughman, B., Moore, J. J., Brown, W. O., Haggerty, J. A., Rockwell, A., Stossmeister, G. J., Williams, S. F., Hernandez, G., Murphy, D. J., Klekociuk, A. R., Reid, I. M., and Ma, J.: The Deep Propagating Gravity Wave Experiment (DEEPWAVE): An Airborne and Ground-Based Exploration of Gravity Wave Propagation and Effects from Their Sources throughout the Lower and Middle Atmosphere, B. Am. Meterol. Soc., 97(3), 425-453, doi:10.1175/Bams-D-14-00269.1, 2016.

Geller, M. A., Alexander, M. J., Love, P. T., Bacmeister, J., Ern, M., Hertzog, A., Manzini, E., Preusse, P., Sato, K., Scaife, A. A., and Zhou, T. H.: A Comparison between Gravity Wave Momentum Fluxes in Observations and Climate Models, J. Climate, 26(17), 6383-6405, doi:10.1175/Jcli-D-12-00545.1, 2013.

Gettelman, A., Hoor, P., Pan, L. L., Randel, W. J., Hegglin, M. I., and Birner, T.: The Extratropical Upper Troposphere and Lower Stratosphere, Rev. Geophys., 49(3), doi:10.1029/2011rg000355, 2011.

Holton, J. R., Haynes, P. H., Mcintyre, M. E., Douglass, A. R., Rood, R. B., and Pfister, L.: Stratosphere-Troposphere Exchange, Rev. Geophys., 33(4), 403-439, doi:10.1029/95rg02097, 1995.

Hoor, P., Fischer, H., Lange, L., Lelieveld, J., and Brunner, D.: Seasonal variations of a mixing layer in the lowermost stratosphere as identified by the CO-O3 correlation from in situ measurements, J. Geophys. Res. Atmos., 107(D5), doi:10.1029/2000JD000289, 2002.

Hoor, P., Gurk, C., Brunner, D., Hegglin, M. I., Wernli, H., and Fischer, H.: Seasonality and extent of extratropical TST derived from in-situ CO measurements during SPURT, Atmos. Chem. Phys., 4(5), 1427-1442, doi:10.5194/acp-4-1427-2004, 2004.

Howard, L. N.: Note on a paper of John W. Miles, J. Fluid Mech., 10(04), 509, doi:10.1017/s0022112061000317, 2006.

Huntrieser, H., Lichtenstern, M., Scheibe, M., Aufmhoff, H., Schlager, H., Pucik, T., Minikin, A., Weinzierl, B., Heimerl, K., Fütterer, D., Rappenglück, B., Ackermann, L., Pickering, K. E., Cummings, K. A., Biggerstaff, M. I., Betten, D. P., Honomichl, S., and Barth, M. C.: On the origin of pronounced O3 gradients in the thunderstorm outflow region during DC3, J. Geophys. Res. Atmos., 121(11), 6600-6637, doi:10.1002/2015jd024279, 2016.

Kaufmann, S., Voigt, C., Jessberger, P., Jurkat, T., Schlager, H., Schwarzenboeck, A., Klingebiel, M., and Thornberry, T.: In situ measurements of ice saturation in young contrails, Geophys. Res. Lett., 41(2), 702-709, doi:10.1002/2013gl058276, 2014.

Kaufmann, S., Voigt, C., Jurkat, T., Thornberry, T., Fahey, D. W., Gao, R. S., Schlage, R., Schäuble, D., and Zöger, M.: The airborne mass spectrometer AIMS - Part 1: AIMS-H2O for UTLS water vapor measurements, Atmos. Meas. Tech., 9(3), 939-953, doi:10.5194/amt-9-939-2016, 2016.

Koch, S. E., Jamison, B. D., Lu, C. G., Smith, T. L., Tollerud, E. I., Girz, C., Wang, N., Lane, T. P., Shapiro, M. A., Parrish, D. D., and Cooper, O. R.: Turbulence and gravity waves within an upper-level front, J. Atmos. Sci., 62(11), 3885-3908, doi:10.1175/Jas3574.1, 2005.

Krautstrunk, M., and Giez, A.: The transition from FALCON to HALO era airborne atmospheric research, In U. Schumann (Ed.), Atmospheric Physics: Background - Methods - Trends, pp. 609-624: Springer-Verlag Berlin Heidelberg, 2012.

Lamarque, J. F., Langford, A. O., and Proffitt, M. H.: Cross-tropopause mixing of ozone through gravity wave breaking: Observation and modeling, J. Geophys. Res. Atmos., 101(D17), 22969-22976, doi:10.1029/96jd02442, 1996.

Lane, T. P., and Sharman, R. D.: Gravity wave breaking, secondary wave generation, and mixing above deep convection in a three-dimensional cloud model, Geophys. Res. Lett., 33(23), doi:10.1029/2006gl027988, 2006.

Langford, A. O., Proffitt, M. H., VanZandt, T. E., and Lamarque, J. F.: Modulation of tropospheric ozone by a propagating gravity wave, J. Geophys. Res. Atmos., 101(D21), 26605-26613, doi:10.1029/96jd02424, 1996.

Mallaun, C., Giez, A., and Baumann, R.: Calibration of 3-D wind measurements on a single-engine research aircraft, Atmos. Meas. Tech., 8(8), 3177-3196, doi:10.5194/amt-8-3177-2015, 2015.

McKenna, D. S., Grooss, J. U., Günther, G., Konopka, P., Müller, R., Carver, G., and Sasano, Y.: A new Chemical Lagrangian Model of the Stratosphere (CLaMS) - 2. Formulation of chemistry scheme and initialization, J. Geophys. Res. Atmos., 107(D15), ACH 4-1-ACH 4-14, doi:10.1029/2000jd000113, 2002a.

McKenna, D. S., Konopka, P., Grooss, J. U., Günther, G., Müller, R., Spang, R., Offermann, D., and Orsolini, Y.: A new Chemical Lagrangian Model of the Stratosphere (CLaMS) - 1. Formulation of advection and mixing, J. Geophys. Res. Atmos., 107(D16), ACH 15-11-ACH 15-15, doi:10.1029/2000jd000114, 2002b.

Miles, J. W.: On the stability of heterogeneous shear flows, J. Fluid Mech., 10(4), 496-508, doi:10.1017/S0022112061000305, 1961.

Moustaoui, M., Mahalov, A., Teitelbaum, H., and Grubišić, V.: Nonlinear modulation of O3 and CO induced by mountain waves in the upper troposphere and lower stratosphere during terrain-induced rotor experiment, J. Geophys. Res., 115(D19), doi:10.1029/2009jd013789, 2010.

Moustaoui, M., Teitelbaum, H., van Velthoven, P. F. J., and Kelder, H.: Analysis of gravity waves during the POLINAT experiment and some consequences for stratosphere-troposphere exchange, J. Atmos. Sci., 56(8), 1019-1030, doi:10.1175/1520-0469(1999)056<1019:Aogwdt>2.0.Co;2, 1999.

Müllemann, A., Rapp, M., and Lübken, F. J.: Morphology of turbulence in the polar summer mesopause region during the MIDAS/SOLSTICE campaign 2001, AdSpR, 31(9), 2069-2074, doi:10.1016/S0273-1177(03)00230-8, 2003.

Pan, L. L., Bowman, K. P., Shapiro, M., Randel, W. J., Gao, R. S., Campos, T., Davis, C., Schauffler, S., Ridley, B. A., Wei, J. C., and Barnet, C.: Chemical behavior of the tropopause observed during the Stratosphere-Troposphere Analyses of Regional Transport experiment, J. Geophys. Res. Atmos., 112(D18), D18110, doi:10.1029/2007jd008645, 2007.

Pavelin, E., Whiteway, J. A., Busen, R., and Hacker, J.: Airborne observations of turbulence, mixing, and gravity waves in the tropopause region, J. Geophys. Res. Atmos., 107(D10), doi:10.1029/2001jd000775, 2002.

Pavelin, E., Whiteway, J. A., and Vaughan, G.: Observation of gravity wave generation and breaking in the lowermost stratosphere, J. Geophys. Res. Atmos., 106(D6), 5173-5179, doi:10.1029/2000jd900480, 2001.

Placke, M., Hoffmann, P., Gerding, M., Becker, E., and Rapp, M.: Testing linear gravity wave theory with simultaneous wind and temperature data from the mesosphere, J. Atmos. Solar-Terr. Phys., 93, 57-69, doi:10.1016/j.jastp.2012.11.012, 2013.

Portele, T. C., Dörnbrack, A., Wagner, J., Gisinger, S., Ehard, B., Pautet, P. D., and Rapp, M.: Mountain Wave Propagation under Transient Tropopsheric Forcing - A DEEPWAVE case study, Mon. Weather Rev., submitted, 2017.

Riese, M., Ploeger, F., Rap, A., Vogel, B., Konopka, P., Dameris, M., and Forster, P.: Impact of uncertainties in atmospheric mixing on simulated UTLS composition and related radiative effects, J. Geophys. Res. Atmos., 117(D16), D16305, doi:10.1029/2012jd017751, 2012.

Schilling, T., Lübken, F. J., Wienhold, F. G., Hoor, P., and Fischer, H.: TDLAS trace gas measurements within mountain waves over northern Scandinavia during the POLSTAR campaign in early 1997, Geophys. Res. Lett., 26(3), 303-306, doi:10.1029/1998gl900314, 1999.

Schumann, U., Weinzierl, B., Reitebuch, O., Schlager, H., Minikin, A., Forster, C., Baumann, R., Sailer, T., Graf, K., Mannstein, H., Voigt, C., Rahm, S., Simmet, R., Scheibe, M., Lichtenstern, M., Stock, P., Rüba, H., Schäuble, D., Tafferner, A., Rautenhaus, M., Gerz, T., Ziereis, H., Krautstrunk, M., Mallaun, C., Gayet, J. F., Lieke, K., Kandler, K., Ebert, M., Weinbruch, S., Stohl, A., Gasteiger, J., Groß, S., Freudenthaler, V., Wiegner, M., Ansmann, A., Tesche, M., Olafsson, H., and Sturm, K.: Airborne observations of the Eyjafjalla volcano ash cloud over Europe during air space closure in April and May 2010, Atmos. Chem. Phys., 11(5), 2245-2279, doi:10.5194/acp-11-2245-2011, 2011.

Shapiro, M. A.: Turbulent Mixing within Tropopause Folds as a Mechanism for the Exchange of Chemical-Constituents between the Stratosphere and Troposphere, J. Atmos. Sci., 37(5), 994-1004, doi:10.1175/1520-0469(1980)037<0994:Tmwtfa>2.0.Co;2, 1980.

Sherwood, S. C., Roca, R., Weckwerth, T. M., and Andronova, N. G.: Tropospheric Water Vapor, Convection, and Climate, Rev. Geophys., 48(2), RG2001, doi:10.1029/2009rg000301, 2010.

Skamarock, W. C., Klemp, J. B., Dudhia, J., Gill, D. O., Duda, M. G., Huang, X.-Y., Wang, W., and Powers, J. G.: A Description of the Advanced Research WRF Version 3, NCAR Technical Note NCAR/TN-475+STR, doi:10.5065/D68S4MVH, 2008.

Smith, R. B., and Kruse, C. G.: Broad-Spectrum Mountain Waves, J. Atmos. Sci., 74(5), 1381-1402, doi:10.1175/jas-d-16-0297.1, 2017.

Smith, R. B., Nugent, A. D., Kruse, C. G., Fritts, D. C., Doyle, J. D., Eckermann, S. D., Taylor, M. J., Dörnbrack, A., Uddstrom, M., Cooper, W., Romashkin, P., Jensen, J., and Beaton, S.: Stratospheric Gravity Wave Fluxes and Scales during DEEPWAVE, J. Atmos. Sci., 73(7), 2851-2869, doi:10.1175/Jas-D-15-0324.1, 2016.

Smith, R. B., Woods, B. K., Jensen, J., Cooper, W. A., Doyle, J. D., Jiang, Q. F., and Grubisic, V.: Mountain waves entering the stratosphere, J. Atmos. Sci., 65(8), 2543-2562, doi:10.1175/2007jas2598.1, 2008.

Solomon, S., Rosenlof, K. H., Portmann, R. W., Daniel, J. S., Davis, S. M., Sanford, T. J., and Plattner, G.-K.: Contributions of Stratospheric Water Vapor to Decadal Changes in the Rate of Global Warming, Science, 327(5970), 1219-1223, doi:10.1126/science.1182488, 2010.

Teitelbaum, H., Moustaoui, M., Ovarlez, J., and Kelder, H.: The role of atmospheric waves in the laminated structure of ozone profiles at high latitude, Tellus A, 48(3), 442-455, doi:10.1034/j.1600-0870.1996.t01-2-00006.x, 1996.

Torrence, C., and Compo, G. P.: A practical guide to wavelet analysis, B. Am. Meterol. Soc., 79(1), 61-78, doi:10.1175/1520-0477(1998)079<0061:Apgtwa>2.0.Co;2, 1998.

Voigt, C., Jessberger, P., Jurkat, T., Kaufmann, S., Baumann, R., Schlager, H., Bobrowski, N., Giuffrida, G., and Salerno, G.: Evolution of CO2, SO2, HCl, and HNO3 in the volcanic plumes from Etna, Geophys. Res. Lett., 41(6), 2196-2203, doi:10.1002/2013gl058974, 2014.

Voigt, C., Schumann, U., Jessberger, P., Jurkat, T., Petzold, A., Gayet, J. F., Krämer, M., Thornberry, T., and Fahey, D. W.: Extinction and optical depth of contrails, Geophys. Res. Lett., 38(11), L11806, doi:10.1029/2011gl047189, 2011.

Voigt, C., Schumann, U., Jurkat, T., Schäuble, D., Schlager, H., Petzold, A., Gayet, J. F., Krämer, M., Schneider, J., Borrmann, S., Schmale, J., Jessberger, P., Hamburger, T., Lichtenstern, M., Scheibe, M., Gourbeyre, C., Meyer, J., Kübbeler, M., Frey, W., Kalesse, H., Butler, T., Lawrence, M. G., Holzäpfel, F., Arnold, F., Wendisch, M., Döpelheuer, A., Gottschaldt, K., Baumann, R., Zöger, M., Sölch, I., Rautenhaus, M., and Dörnbrack, A.: In-situ observations of young contrails - overview and selected results from the CONCERT campaign, Atmos. Chem. Phys., 10(18), 9039-9056, doi:10.5194/acp-10-9039-2010, 2010.

Wagner, J., Dörnbrack, A., Rapp, M., Gisinger, S., Ehard, B., Bramberger, M., Witschas, B., Chouza, F., Rahm, S., Mallaun, C., Baumgarten, G., and Hoor, P.: Observed versus simulated mountain waves over Scandinavia – improvement of vertical winds, energy and momentum fluxes by enhanced model resolution?, Atmos. Chem. Phys., 17(6), 4031-4052, doi:10.5194/acp-17-4031-2017, 2017.

Whiteway, J. A., Pavelin, E. G., Busen, R., Hacker, J., and Vosper, S.: Airborne measurements of gravity wave breaking at the tropopause, Geophys. Res. Lett., 30(20), doi:10.1029/2003gl018207, 2003.

WMO: Meteorology - A three-dimensional science, WMO Bulletin, 6, 134-138, 1957.

Woods, B. K., and Smith, R. B.: Energy Flux and Wavelet Diagnostics of Secondary Mountain Waves, J. Atmos. Sci., 67(11), 3721-3738, doi:10.1175/2010jas3285.1, 2010.

Woods, J. D.: On Richardson's Number as a Criterion for Laminar-Turbulent-Laminar Transition in the Ocean and Atmosphere, Radio Sci., 4(12), 1289-1298, doi:10.1029/RS004i012p01289, 1969.

Wright, C. J., Hindley, N. P., Moss, A. C., and Mitchell, N. J.: Multi-instrument gravity-wave measurements over Tierra del Fuego and the Drake Passage - Part 1: Potential energies and vertical wavelengths from AIRS, COSMIC, HIRDLS, MLS-Aura, SAAMER, SABER and radiosondes, Atmos. Meas. Tech., 9(3), 877-908, doi:10.5194/amt-9-877-2016, 2016.

Young, K., Hock, T., and Martin, C.: DEEPWAVE 2014 Dropsonde Data Quality Report, UCAR/NCAR - Earth Observing Laboratory, 2014.

Zhang, F. Q., Wei, J. H., Zhang, M., Bowman, K. P., Pan, L. L., Atlas, E., and Wofsy, S. C.: Aircraft measurements of gravity waves in the upper troposphere and lower stratosphere during the START08 field experiment, Atmos. Chem. Phys., 15(13), 7667-7684, doi:10.5194/acp-15-7667-2015, 2015.

Zondlo, M. A., Paige, M. E., Massick, S. M., and Silver, J. A.: Vertical cavity laser hygrometer for the National Science Foundation Gulfstream-V aircraft, J. Geophys. Res. Atmos., 115(D20), doi:10.1029/2010jd014445, 2010.

Table 1. Measurement range, accuracy and precision for the CR-2 hygrometer.

Measurement range	Accuracy	Precision
50-500 ppmv	9%	1%
10-50 ppmv	9-12%	2%
<10 ppmv	>12%	>2%

Table 2. Overview of the research flights on 4 July 2014 (FF = Falcon research flight, RF = GV research flight).

Aircraft	Flight no.	Flight time (UTC)	Dropsonde launches
DLR Falcon 20E	FF04	02:46 – 06:09	--
DLR Falcon 20E	FF05	07:23 – 11:00	--
NSF/NCAR Gulfstream V	RF16	05:59 – 12:55	15 (mountain transect); 1 (east of South Island)

Table 3. Vertical flux divergence of water vapor for the combined research flights FF04, FF05 and RF16. The results are shown for two horizontal wavelength ranges.

Flight no.	Leg number	Altitude (km)	$\frac{\partial(\overline{w'H_2O'})}{\partial z}$ (ppmv s^{-1}) $\boldsymbol{\lambda_h = 300\ m - 80\ km}$	$\frac{\partial(\overline{w'H_2O'})}{\partial z}$ (ppmv s^{-1}) $\boldsymbol{\lambda_h = 22\ km - 80\ km}$
FF04	leg1→leg2	7.7 – 8.9	3.0E-02	-2.9E-02
FF04	leg2→leg3	8.9 – 10.8	-1.5E-03	-1.1E-03
FF05	leg1→leg2	7.7 – 8.9	5.2E-02	4.6E-02
FF05	leg2→leg3	8.9 – 10.8	-3.2E-03	-2.2E-03
FF05/RF16	leg3 (FF05)→leg4 (RF16)	10.8 – 12.0	2.4E-04	-9.0E-04
RF16	leg4→leg5	12.0 – 13.0	-7.9E-05	-5.8E-05

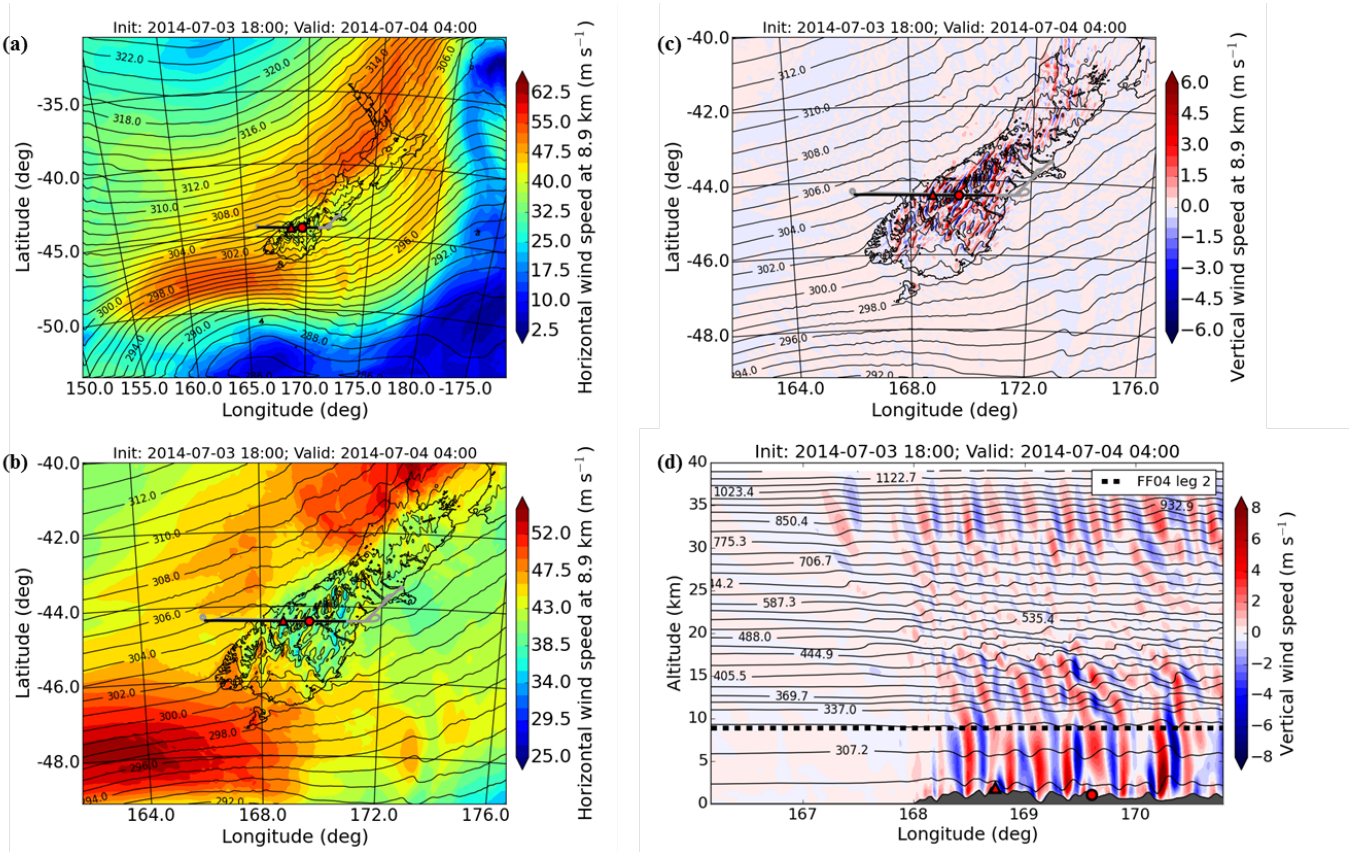

Figure 1. Synoptic situation on 4 July 2014 at 04 UTC simulated by WRF: (a) horizontal wind speed at 8.9 km (altitude of DLR Falcon flight FF04 leg 2) for New Zealand, (b) horizontal wind speed over the South Island of New Zealand (zoom of (a)), ~~(a, b) and v~~(c) vertical wind speed ~~(c)~~ at 8.9 km over the South Island of New Zealand and (d) cross section of the vertical wind speed along the flight leg. ~~(altitude of DLR Falcon flight FF04 leg 2) simulated by WRF~~. Contour lines represent the potential temperature at 8.9 km (a – c) and over the altitude (d). The thick black line in (a – c) displays the cross-mountain flight path and the grey line shows the whole flight path of the DLR Falcon flight FF04. The thick black dashed line in (d) indicates the altitude of the of the second flight leg of FF04 and the grey area at the bottom displays the topography. The red dot in ~~(b, c)~~all panels marks the position of the dropsonde launch from the GV at 08 UTC (see Figure 7) and the red triangle marks the position of Mt. Aspiring.

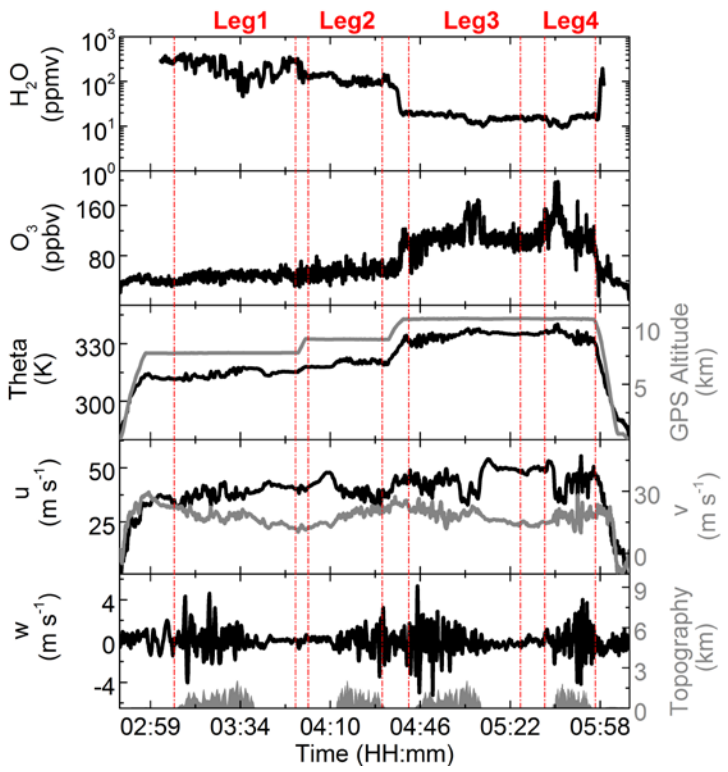

Figure 2. DLR Falcon flight FF04 on 4 July 2014 above the Southern Alps: time series of observations during the mountain wave event. Water vapor mixing ratio (from CR-2), ozone mixing ratio, potential temperature and flight altitude (grey) as well as zonal wind, meridional wind (grey), vertical wind and topography (grey area at the bottom) are shown. Flight legs are separated by dashed red lines.

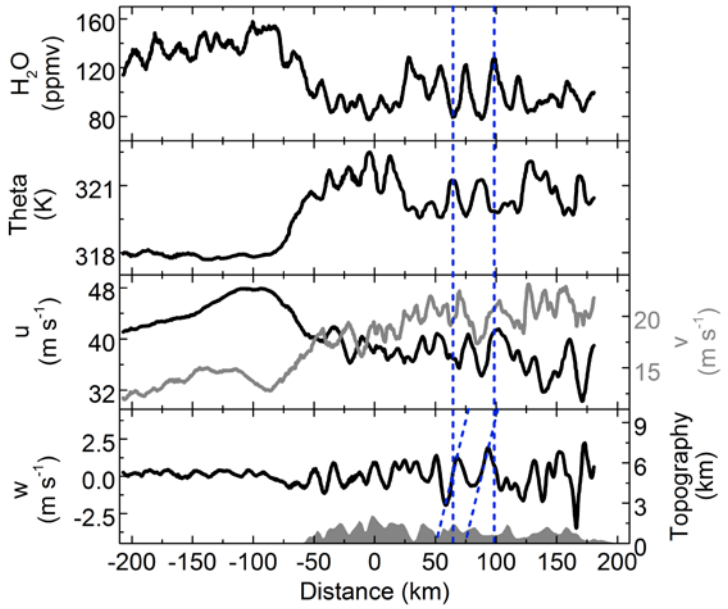

Figure 3. A portion of the time series of the DLR Falcon flight FF04 on 4 July 2014 shown in Figure ~~1~~2. The measurements were taken during the second flight leg at 8.9 km altitude over the South Island of New Zealand. The distance refers to Mt. Aspiring as the highest summit during this mountain transect (west to east). The vertical blue dashed lines mark single wave events. ~~and t~~The diagonal blue dashed lines in the bottom panel connect the maximum or minimum of the vertical wind motion with the respective maximum or minimum in the perturbations of water vapor and theta which displays the phase shift between these parameters. ~~vertical wind motion and perturbations in water vapor and theta.~~

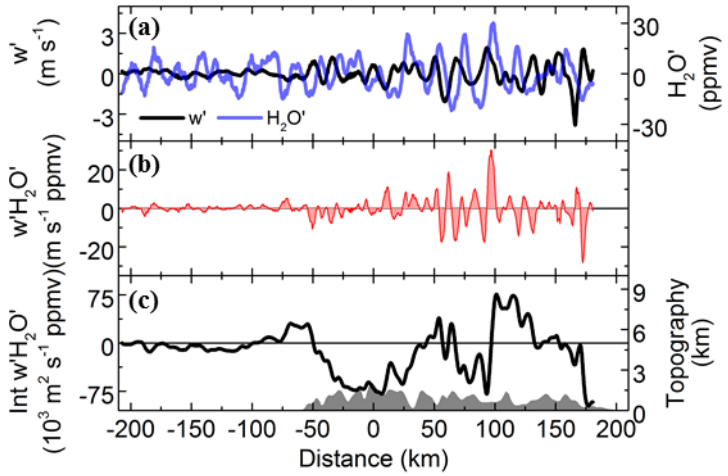

Figure 4. Same flight leg as in Figure 3. Shown are components of the vertical water vapor flux. The vertical wind perturbation (black) and the water vapor perturbation (blue) in (a) are combined to the local vertical water vapor flux w'H_2O' (b). The bottom panel (c) shows the integrated vertical water vapor flux $\int$w'H_2O'dx and the topography.

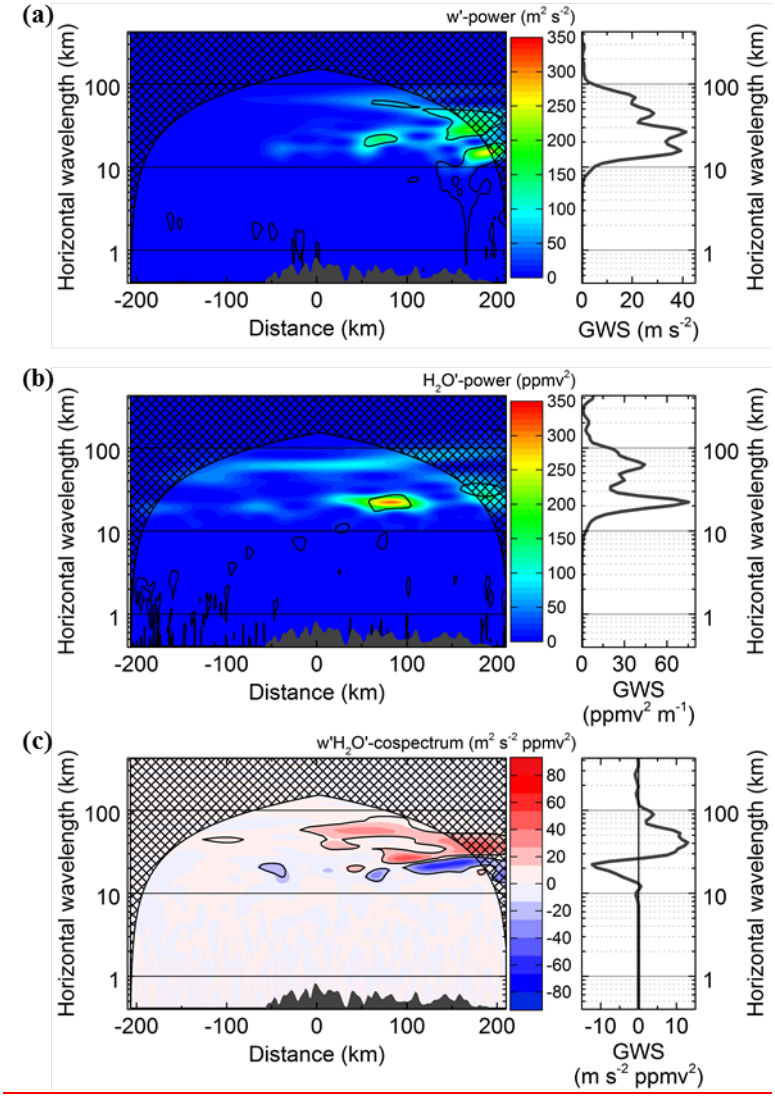

Figure 5. Wavelet analysis of the second flight leg of the DLR Falcon flight FF04 shown in Figure 2: (a) power spectrum of vertical wind perturbation w', (b) power spectrum of water vapor perturbation H_2O', and (c) cospectrum of the vertical water vapor flux w'H_2O'. The right panels show the corresponding global wavelet spectrum (GWS). Thin black lines around coloured areas are the 95 % confidence level; the crosshatched area is the COI. The topography (maximum mountain height of 2049 m) is represented by the dark grey area in the bottom of each panel.

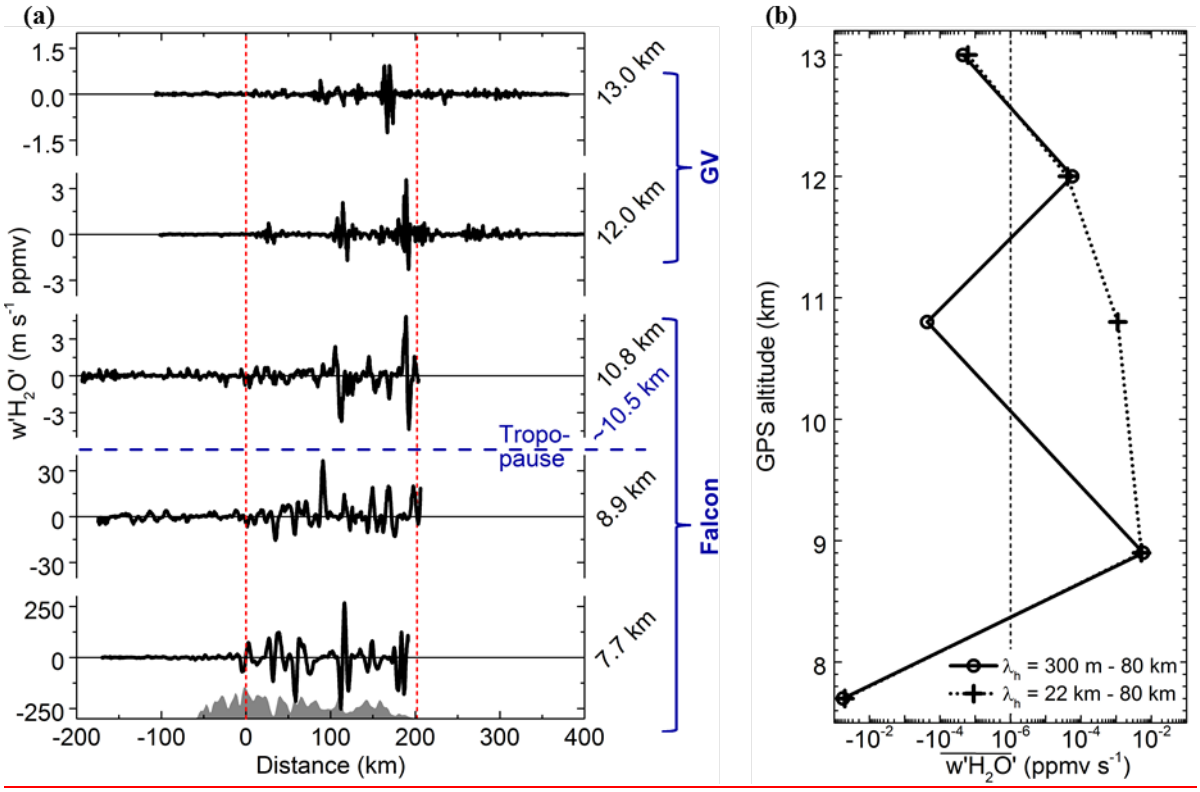

Figure 6. (a) Vertical water vapor fluxes using data from DLR Falcon flight FF05 (lower three panels) and NSF/NCAR GV flight RF16 (upper two panels) on 4 July 2014. The fluxes are shown for different flight altitudes over the topography of the Southern Alps. The approximate height of the tropopause at 10.5 km is ~~marked with~~displayed by the dashed blue line. The red dashed lines mark the region that is used to get the water vapor fluxes shown in panel (b). (b) Vertical profile of the water vapor fluxes integrated over the mountain region with highest mountain wave activity. The profiles are shown for horizontal wavelengths between 300 m and 80 km (solid line) and between 22 km and 80 km (dashed line).

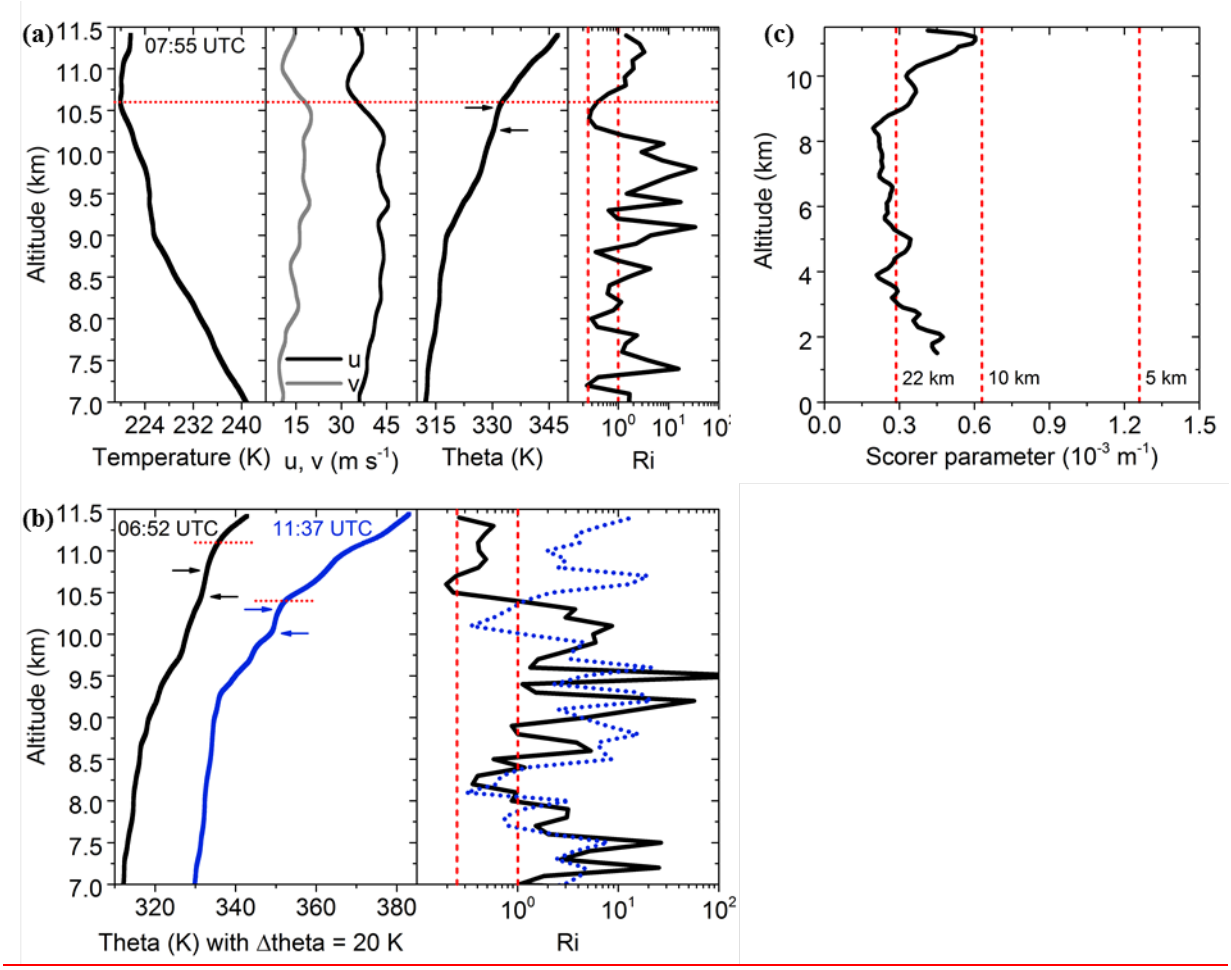

Figure 7. Dropsonde launches from 12.2 km height during the GV flight RF16. The panels in (a) represent the profiles of temperature, potential temperature, horizontal wind components and Richardson number for GPS altitudes from 7.0 to 11.5 km for a dropsonde at 07:55 UTC. The lower panel (b) shows the profiles of potential temperature and Richardson number for dropsondes launched at the same location as the dropsonde from (a) at 06:52 UTC (black) and 11:37 UTC (blue). The red dashed lines in the right panel show critical Ri at 0.25 and 1.0, the arrows in the theta panel denote regions with suggested turbulence. Horizontal red dotted lines in (a) and (b) mark the height of the thermal tropopause. (c) Vertical profile of the Scorer parameter ℓ (smoothed with an running average) derived from the dropsonde at 07:55 UTC (see panel (a)). The red dashed lines show vertical profiles of the critical horizontal wavelengths $2\pi/\ell$ of 5 km, 10 km and 22 km.

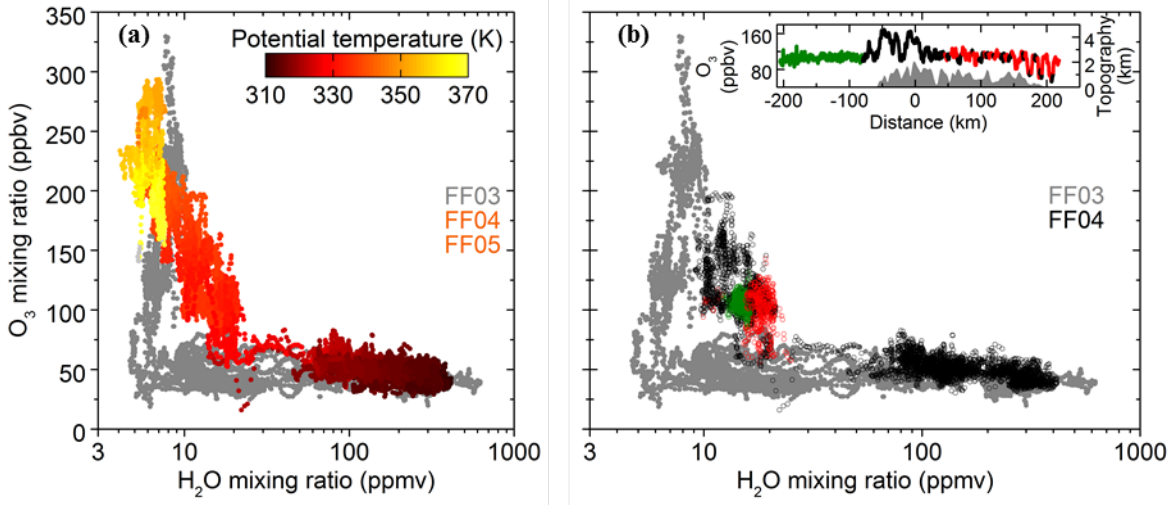

Figure 8. H_2O-O_3 correlation for three Falcon flights: (a) FF04 and FF05 in mountain wave conditions and FF03 in unperturbed conditions. Potential temperature is colour-coded for FF04 and FF05. (b) FF04 with a red-marked region for potential temperatures between 329 and 334 K that correspond to regions where turbulence in the dropsonde data of flight RF16 was observed. The inlay in (b) gives the ozone mixing ratio of flight FF04 leg 3 at 10.8 km. The red data points show the localisation of potential temperatures between 329 and 334 K in the ozone data and green data points mark the upstream region of this flight leg.